DIPLOMARBEIT

Small Field Irradiation with Proton Beams

Zur Erlangung des akademischen Grades

Diplom-Ingenieurin

im Rahmen des Studiums

Biomedical Engineering

ausgeführt am

Atominstitut

Fakultät für Physik

Technische Universität Wien

in Zusammenarbeit mit der

Universitätsklinik für Radioonkologie

Medizinische Universität Wien

eingereicht von

Aramesadat Sotoudegan

Matrikelnummer 11701190

Betreuer: Univ. Prof. Dipl.-Ing. Dr.techn. Dietmar Georg

Mitwirkung: Dr. Monika Clausen

Wien, 01.12.21

_____   _____

Unterschrift Studentin   Unterschrift Betreuer

1

2

Abstract

Particle beam therapy, which uses accelerated protons and carbon ions to treat cancer, has become more widely available during recent decades. Due to the increasing dose deposition at the end of the particle's range (Bragg Peak) and the sharp fall-off after it, compared to the conventional photon and electron beam radiotherapy, particle therapy has an advantage of treating tumors located close to the organs at risk (OAR) while sparing efficiently the surrounding healthy tissue.

Using small animal models is essential to improve understanding of radiation effects in tissues. At MedAustron (Wiener Neustadt, Austria), it is planned in the near future to irradiate small animals in the frame of pre-clinical radiobiological research. The equipment (software and hardware) designed for patients has certain limitations and has to be adapted for small targets relevant to small animals. Accordingly, the main focus of this work was given to the irradiation of small fields with proton beams and to the investigation of using the existing patient-developed equipment for small field irradiation to apply it for in vivo animal studies. This work is part of the preparatory work intended to establish the whole irradiation workflow for radiobiological in vivo studies at MedAustron.

This thesis is based on a simple phantom, made of polymethylmethacrylate (PMMA) material, representing in its size a small animal (e.g., mouse). The small targets inside the phantom were delineated, the doses were calculated and the treatment plans were created in the clinical treatment planning system (TPS-Raystation, Raysearch, Sweden). Experiments were performed in different setups. Since the beams are rather large in comparison to the target size, apertures are required to limit the irradiation field. Therefore, the apertures as beam shaping devices, with the openings of 1.5 cm and 1.2 cm in diameter, were tested. Moreover, the typical targets in small animals are located at shallow depths and a pre-absorber has to be included in the beam pathway to

reduce the penetration depth of clinical beams. Two different types of pre-absorbers, i.e. either a bolus or a range shifter, were employed to find the optimal setup for the small field irradiation. In addition to different apertures and different pre-absorbers investigation, small targets with 1.2 cm and 0.8 cm radius were analyzed. The positioning accuracy of the aperture was also tested. Finally, an importance of including the aperture into the treatment planning process was addressed. During the irradiation, the absorbed doses were measured with two different detector types: a microDiamond detector (active detector) and EBT3 films (passive detector).

The investigation in the setups with apertures of different sizes yielded that the dose distribution in the target was homogeneous and the lateral penumbra was significantly reduced. Based on the experimental approach with detectors, the dose was distributed homogeneously inside the target when the range shifter was used as the pre-absorber. When the bolus was placed in front of the phantom as pre-absorber, more dose was concentrated at the center of the target and the lateral dose profile became dome-shaped with a 10% higher dose than the prescribed dose. The target dose inhomogeneities may increase the risk of overdosing and underdosing different areas within the target volume. Regarding the target sizes, comparable dose distributions and lateral penumbras were present in both investigated targets of 0.8 cm and 1.2 cm in diameter. The positioning accuracy of the aperture relative to the phantom and the target was important and misplacements of more than 1mm led to fairly large differences in target doses. Last but not least, not considering the aperture in the TPS led to target overdose of 12%. In addition, when the aperture was not considered in the treatment planning process and simply placed in front of the phantom, three times larger lateral penumbra was observed.

To conclude, the clinical beamline has to be adapted for small (< 2cm) and shallow field irradiation relevant in small animals using a collimator and a pre-absorber. The use of clinical TPS based on Monte Carlo dose calculations proved to be appropriate for target sizes down to 0,8 cm (diameter). The accurate positioning of the setup is an important aspect for small field irradiation.

Zusammenfassung

Die Teilchentherapie gewann in den letzten Jahrzenten immens an Bedeutung, sie bezeichnet die Verwendung von beschleunigten Protonen oder Kohlenstoffionen zur Behandlung von Tumoren. Wegen der zunehmenden Dosisdeposition am Ende der Partikelreichweite (Bragg Peak) und dem starken Abfallen danach, im Vergleich zur konventionellen Photon- und Elektronstrahlentherapie, ist die Teilchentherapie vorteilhafter um Tumorzellen in der Nähe von lebensnotwendigen Organen effizient zu behandeln und dabei gesunde Zellen bestmöglich zu schonen. Vorteile der Teilchentherapie gegenüber der konventioneller Photonentherapie sind die zunehmende Dosisdeposistion am Ende Reichweite (Bragg Peak) und dem darauffolgenden starken Dosisabfall. Somit ist es möglich Tumoren in der Nähe von Risikoorganen zu behandeln und das umliegende gesundes Gewebe zu effizient zu schonen.

Die Verwendung von Kleintiermodellen ist essenziell, um die Ergebnisse der Strahlentherapie zu verbessern. Bei MedAustron (Wiener Neustadt, Niederösterreich, Österreich) ist in naher Zukunft geplant Kleintiere im Rahmen der präklinischen Forschung zu bestrahlen. Das auf den Menschen abgestimmte Equipment (Software und Hardware) für die Teilchentherapie muss zunächst für Kleintiere adaptiert werden. Diese Diplomarbeit ist Teil der vorbereitenden Arbeit, mit denen der gesamte Bestrahlungsworkflow für strahlenbiologische in-vivo-Studien bei MedAustron etabliert werden soll.

Diese Arbeit basiert auf einem einfachen Phantom aus Polymethylmethacrylat (PMMA) in der Größe einer Maus. In dem für Patienten entwickelten Bestrahlungsplanungssystem (TPS-Raystation, Raysearch, Schweden), wurden die kleinen Zielgebiete innerhalb des Phantoms abgegrenzt, die Dosisverteilung berechnet und die Behandlungspläne erstellt. Die Experimente wurden in verschiedenen Setups

durchgeführt. Da die Strahlgröße im Vergleich zur Zielgröße relativ groß ist, müssen Aperturen verwendet werden, um das Bestrahlungsfeld zu begrenzen. Daher wurden für die Formung des Strahls Aperturen mit den Öffnungsgrößen von 1,5 cm und 1,2 cm getestet. Darüber hinaus befinden sich die typischen Ziele bei Kleintieren in geringer Tiefe und daher ist es, um die Eindringtiefe zu reduzieren, nötig einen Vorabsorber in den Strahlengang zu integrieren. Um den optimalen Aufbau für die Bestrahlung von kleinen Feldern zu bestimmen wurde, sowohl ein Bolus als auch ein Range Shifter als Vorabsorber untersucht. Zusätzlich wurden kleine Zielgebiete mit 1,2 cm und 0,8 cm Radius, sowie die Positioniergenauigkeit der Blende analysiert. Während der Bestrahlung wurden die Energiedosen mit zwei verschiedenen Detektortypen gemessen: microDiamond-Detektor (aktiver Detektor) und EBT3-Filme (passiver Detektor).

Die Untersuchung der Setups mit unterschiedlich großen Aperturen ergab, dass die Dosisverteilung im Ziel homogen und die laterale Penumbra reduziert war.

Unter Verwendung eines Range Shifters als Vorabsorber war die Dosis homogen im Ziel verteilt, während bei der Verwendung des Bolus mehr Dosis in der Mitte des Zielvolumens gemessen wurde. Zusätzlich konnte festgestellt werden, dass das laterale Dosisprofil kuppelförmig wird und die Dosis um 10% erhöht war. Die Inhomogenitäten der Dosis im Zielgebiet können das Risiko einer Über- und Unterdosierung verschiedener Bereiche innerhalb des Zielvolumens erhöhen. Hinsichtlich der Größen der Zielgebiete waren die Dosisverteilungen sowie die lateralen Halbschatten zwischen 0,8 cm und 1,2, cm Durchmesser vergleichbar. Die Positionierungsgenauigkeit der Blende relativ zum Phantom sowie zum Zielgebiet war wichtig und Fehlstellungen von über 1 mm führten zu großen Unterschieden in den Dosisverteilungen. Nicht zuletzt, führte die Weglassen der Blende im TPS zu einer Überdosierung von 12%. Wenn die Apertur bei der Behandlungsplanung nicht berücksichtigt und einfach vor dem Phantom platziert wurde, wurde außerdem eine dreimal größere laterale Halbschatten beobachtet.

Zusammenfassend muss die klinische Strahllinie für kleine (< 2 cm) und oberflächliche Strahlung, die bei Kleintieren relevant ist, unter Verwendung eines Kollimators und eines Vorabsorbers, angepasst werden. Der Einsatz klinischer TPS auf Basis von Monte Carlo Dosisberechnung erwies sich für Zielgrößen bis zu 0.8 cm (Durchmesser) als

sinnvoll. Die genaue Positionierung des Setups ist ein wichtiger Aspekt bei der Bestrahlung mit kleinen Feldern.

Acknowledgement

My sincere gratitude goes to my supervisor Univ. -Prof. Dr. DI Dietmar Georg, who gave me the opportunity to work on my Master's thesis at the Department of Radiation Oncology at the Medical University of Vienna and a workplace for my studies at MedAustron in Wiener Neustadt.

I owe my deepest gratitude to my co-supervisor Dr. Monika Clausen for guiding me through every aspect of this work and for her tireless support, patience and time. I also want to thank you for the amazing shifts that we had together. Additionally, I would like to thank all people from MedAustron I had a chance to work with, particularly Hugo Palmans for supporting me and for sharing his knowledge and experience.

Moreover, I want to express my profound gratitude to my parents, who made it possible for me to study in the first place, also Firouzeh, Haschem and my sister Azin. Without your love and encouragement, I would never have come this far!

Finally, I want to thank my beloved husband Sahand for the endless support and motivation during a stressful and hard times.

Contents

List of Figures

List of Tables

Chapter 1

Introduction

This chapter provides a brief overview of the basics of radiation oncology and more particularly on particle beam therapy. In addition, an introduction of detectors used in particle beam therapy for small fields will be presented, with the main focus on Gafchromic films and diamond detector. In the end, the MedAustron the particle beam therapy facility, where all measurements in this thesis were performed there, will be briefly introduced.

1.1 Basics of Radiation Therapy

Cancerous cells have the ability to divide incessantly, proliferate and develop a tumor, which is a cluster of cancerous cells. Some of these cells have the ability to spread through the body, resulting in distant secondary tumors, known as metastasis [1]. Ionizing radiation breaks the DNA of cells to cease cell growth and cell division. As a result, cells are unable to repair themselves and go to apoptosis. An approach of ionizing radiation to treat cancer is called radiation therapy. Radiation therapy is one of the three main options for cancer treatment among with surgery and systemic therapy, such as chemotherapy and hormone therapy [2]. Depending on the type and stage of the malignancy, one of these methods or occasionally a combination of these methods

are used to treat the disease. Contrary to chemotherapy, radiation therapy is targeted and the beams are shaped to match the tumor form. Radiation therapy seeks to administer a prescribed dose while causing the least damage to underlying normal tissue [3].

Based on the location of the radiation source relative to the patient, the delivery of radiotherapy is subdivided into three categories:

- Unsealed source radiotherapy
- Sealed source radiotherapy
- External beam radiotherapy

In unsealed source radiotherapy, radiopharmaceuticals are injected or ingested. The common applied source is ^{131}I. In sealed radiotherapy, where commonly ^{131}Cs, ^{137}Cs, ^{60}Co and ^{192}Ir are used, the source is applied directly inside or around the tumor. In external beam radiotherapy (EBRT), the radiation source is located outside of the patient. In EBRT X-rays and electron beams are the most widely used sources as they are easy to produce [4].

Photon based radiation therapy has become the most utilized therapy against cancer in hospitals and medical institutes due to the physical properties and relatively low cost of equipment. Nonetheless, the utilization of charged particles is emerging [5]. Figure 1-1 depicts the photon beam dose-depth profile, which is characterized by an initial build-up to a maximum value followed by an exponential decrease. In case of electron beams, the maximum dose deposition occurs at shallow depths. The dose deposition drops significantly after the maximum. Therefore, electron beams are efficient for treating superficial tumors. The depth-dose profiles of heavier charged particles (protons and ions) are very beneficial for treating profound tumors with significantly reducing total irradiated volume. Particle beams release most of their energy directly into the tumors [6]. As shown in Figure 1-1 there is an almost constant dose before the Bragg peak and afterwards an almost immediate fall-off behind the maximum. External beam radiotherapy with heavy charged particles will be discussed in detail in the following section.
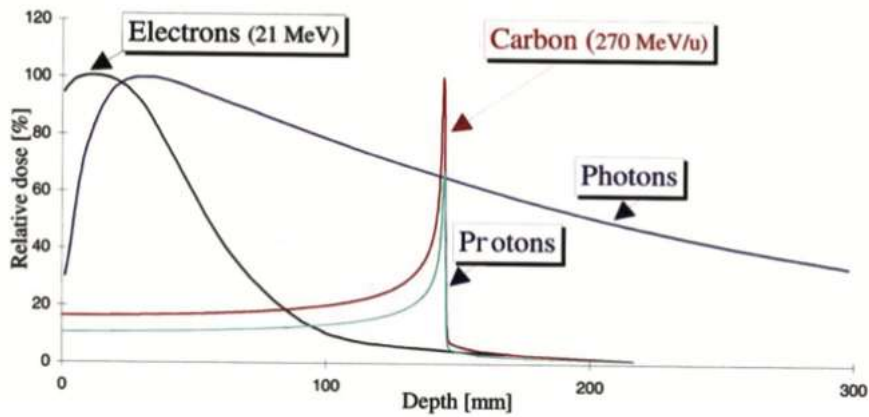
Figure 1-1: Depth-dose curve of electron, photon, proton and carbon beams [7]

1.2 Particle Radiation Therapy

In particle beam therapy protons or light ions, such as carbon ions, are used for treatment [5]. The most common form of particle therapy is proton therapy. Cyclotrons or synchrotrons are used to accelerate the particles and their energy is adjusted to the desired energy level directly in the accelerator or with an energy degrader system. Protons that are accelerated to therapeutic energy ranges from 70 to 250 MeV, are transported to treatment rooms with fixed beamlines or rotating gantries.

As indicated previously, when comparing to photon or electron beams, charged particles have different dosimetric properties. The dose rises gradually with depth and the maximal dose is deposited near the end of the particle beam. Not only is the entrance dose lower than the one in photon radiotherapy, but also the Bragg peak and sharp fall-off after the peak, a higher dose can be delivered to the tumor while the surrounding tissues, especially behind the tumor, are left unirradiated. Particle beam therapy is beneficial for tumors that are close to organs at risk, as well as pediatric patients [8]. The physical properties of carbon ions are similar to protons. They have sharper lateral penumbra as well as dose fall-off, which is an advantage but contrary to protons, carbon ions deliver small doses beyond the Bragg peak (Figure 1-1).

The dimension of the targets is commonly broader than the width of one unmodulated Bragg peak, hence a superposition of Bragg peaks with divergent energy range and intensity is used. This results in an extended region of uniform dose, which is called spread-out Bragg peak (SOBP). In Figure 1-1 only monoenergetic beams are shown, while a SOBP which is a more realistic approach in cancer treatment is shown in Figure 1-2.
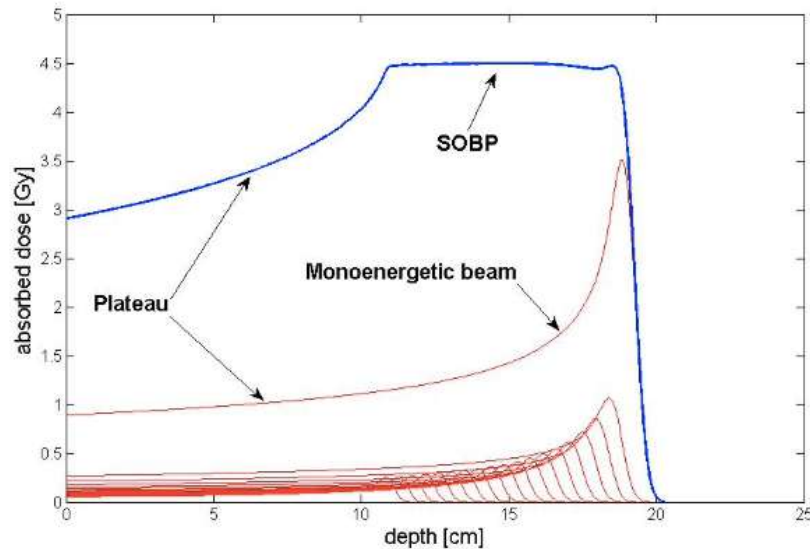
Figure 1-2: Spread out Bragg peak dose depth distribution for protons (blue line), generated by superposition of a group of monoenergetic proton beams (red lines) [9]

A disadvantage of particle therapy is that the accelerator systems are expensive, they need more space, shielding, and maintenance. These factors increase the costs of these types of therapy. Carbon ion radiotherapy requires even larger equipment to accelerate the beam and therefore, is more expensive and less available than proton radiotherapy.

1.3 Interaction of Charged Particles with Matter

When a charged particle passes through an absorber, it encounters Coulomb interactions with nuclei and orbital electrons of the absorber atoms. Depending on the magnitude of the impact parameter (b) of the charged particle and the atomic radius (a) of an absorber atom, these interactions can be divided into three groups [10]:

1. **Coulomb force interaction of the charged particle with the absorber atom's nuclear field for ($b \ll a$):** when the magnitude of the impact parameter b of a charged particle is considerably less than atomic radius a of absorber atom, the charged particle interacts with the nucleus and experiences elastic or inelastic scattering followed by a change in direction. Most of these interactions are elastic. Even though the particle is scattered by the nucleus, only a small part of its kinetic energy is transferred. The minority of these interactions are inelastic. The energy of a charged particle is transferred to x-ray emission in a remarkable quantity. This type of interaction is called radiation collision.

2. **Coulomb force interaction of charged particle with the orbital electron of absorber atom for ($b \approx a$):** when the magnitude of the impact parameter b of a charged particle is approximately near to atomic radius a of an absorber atom, the charged particle undergoes an interaction with orbital electron of the absorber atom. In this interaction a large amount of kinetic energy is transferred to an orbital electron so that the orbital electron leaves the atom as δ-ray. The possibility of occurrence of this type of interaction is relatively low. This interaction is known as hard or close collision.

3. **Coulomb force interaction of charged particle with the orbital electron of absorber atom for ($b \gg a$):** when the magnitude of the impact parameter b of a charged particle is extremely larger than the atomic radius a of an absorber atom, the charged particle interacts with the whole atom and the whole bound of electrons. A relatively limited quantity of kinetic energy is transferred from the charged particle to the electron. Nevertheless, the possibility of these interactions is high. This type of interaction is referred to as soft or distant collision.

Figure 1-3 shows radiation collision, hard collision and soft collision, where b is the impact parameter of charged particle trajectory and a is the atomic radius of the absorber atom.
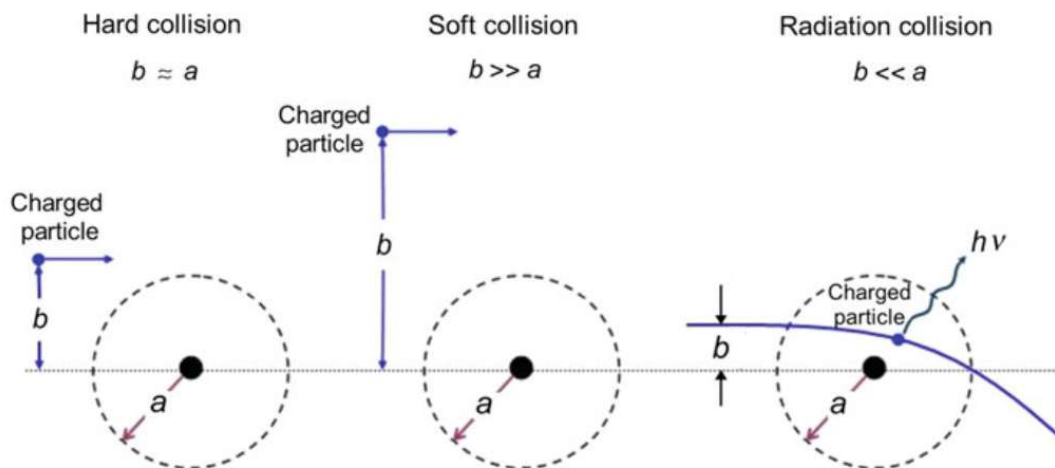
Figure 1-3: Different types of charged particle collision with an atom. Hard (close) collision when ($b \approx a$), soft (distant) collision when ($b \gg a$) and radiation collision when ($b \ll a$) [10]

LET and Relative Biological Effectiveness

Coulomb interactions cause atoms along the path of a charged particle to be excited and ionized. The transferred energy to matter per unit path length is called linear energy transfer (equation 1-1). The stopping power is the energy loss of heavy particles per unit path length (equation 1-2) [11].

$$LET = \frac{dE}{dx} \tag{1-1}$$

$$S = -LET = -\frac{dE}{dx} = \frac{4\pi e^4 Z_t Z_p^2}{m_e v^2}\left[\ln\frac{2m_e v^2}{\langle I \rangle} - \ln(1-\beta^2) - \beta^2 - \frac{C}{Z_t} - \frac{\delta}{2}\right] \tag{1-2}$$

Where Z_p and Z_t are the atomic number of the projectile and the target, m_e and e are the mass and charge of the electron, $\langle I \rangle$ is mean ionization energy of atom$_{target}$, v is the velocity of the projectile and β is $\frac{v}{c}$.

One of the important measurements for the effect of radiation on tissue is relative biological effectiveness (RBE). An equal physical dose of different radiation types produces unequal biological effects. The relative biological effectiveness is used to compare the effect of various kinds of radiation. It is described as the ratio of absorbed

dose of a reference radiation and dose of different radiation having the same biological effect [12]. Based on numerous in-vitro and animal investigations, protons have 10% higher biological effectiveness relative to photons [6]. RBE for protons is estimated to be constant and equal to 1.1 while carbon ions have a higher RBE of up to 3.4.

1.4 Dosimetry

Energy is transmitted from ionizing radiation to matter during irradiation. The term "dose" refers to the effect of this energy on the material. The measurement of the absorbed energy by the material is defined as dosimetry [12, 13], in other words, radiation dosimetry is the measurement of quality and quantity of ionizing radiation. One of the most important quantities in radiation dosimetry is the absorbed dose. Absorbed dose or dose rate is the energy deposited in material from any type of ionizing radiation per unit mass. It is defined as:

$$D = \frac{d\bar{\varepsilon}}{dm} \qquad\qquad (1-3)$$

Where $d\bar{\varepsilon}$ is the mean energy deposited by ionizing radiation to matter and dm is the mass of matter in volume, measured in Gray (Gy), which is equal to J/kg [12, 14].

For the purpose of measuring this quantity several types of measuring systems are available, for example, ionization chambers, solid state detectors e.g., diamond detector, GAFchromic films or thermoluminescence dosimeters (TLDs). These detectors can be divided into two categories: active detectors, also called real time detectors, as they provide an audible or visual indication of the dose level in real time on a portable electrometer to demonstrate the presence of radiation. Mainly ionizing chambers belong to this group. The other group being passive detectors, record the measured dose and report it after evaluation. They do not provide direct readouts, e.g. thermoluminescent materials (TLDs) or radiochromic films.

1.5 Dosimeters

1.5.1 Active Dosimeters

An ionization chamber is an active detector that consists of a gas- or liquid-filled chamber and two electrodes. The shape of the electrodes is determined by the type of the chamber. Between the electrodes, there is a potential that leads to the creation of an electric field. Ionizing radiation causes ionization of gas and ion-pairs creation inside the gas-filled volume. Due to the application of an electric field positive and negative ions move to corresponding electrodes and generate ionization current. This electric field should neither be so faint that causes ion recombination nor so powerful that causes subsequent collisions [15, 16]. By detecting the secondary charges in the chamber with an electrometer, the deposed energy in the detector is measured. This charge is proportional to the number of created ions and radiation dose [17, 18].

Another type of active detector is microDiamond detector. The microDiamond detector was developed by the University of Rom Tor Vergata and commercialized by PTW [19, 20]. It is the first available single crystal diamond detector suitable for clinical dosimetry. PTW microDiamond detector has a small active volume, is water equivalent and thus suitable for small field dosimetry for fields smaller than 1 cm^2 [19]. More details can be found in subsection 2.5.2.

Figure 1-4 depicts the basic principles of PTW diamond detector operation. Generated positive and negative charges produced by incident radiation are separated by the field of the diode. The produced current can be measured by an electrometer. There is no need for external bias voltage.
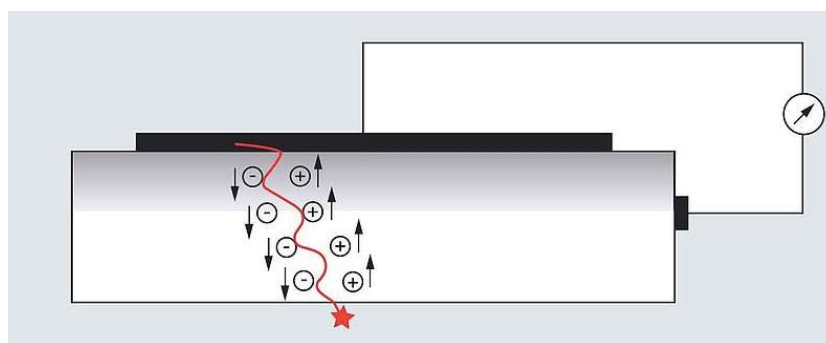
Figure 1-4: Basic operation principles of PTW microDiamond detector [20]

20

1.5.2 Passive Dosimeters

One type of passive detector is the Thermoluminescent dosimeter (TLD). TLDs are ionizing radiation detector crystals. After being irradiated, a reading of the detectors is performed by heating the detector and detecting the light released by the crystal. The light can be detected with a photomultiplier. The intensity of emitted light from the crystal is proportional to the absorbed dose. Heat is not a primary energy source. The interaction of ionizing radiation with crystals is the origin of energy. Some types of TLDs can be used in the dosimetry of small fields. TLDs are available in a variety of shapes and sizes. The defined target size in this project was 1.2 cm and 0.8 cm which makes TLDs not suitable for this thesis [21].

Another example of passive detectors would be radiochromic films, that is used to investigate 2D dose distributions. In comparison with radiographic films, radiochromic films are not sensitive to light and are self-developing. EBT3 and EBT-XD films can be used for 0.2 to 10 Gy and 0.4 to 40 Gy (low dose range dosimetry) and MD and HD can be used for mid ranges (<100 Gy) and high dose ranges (<1000 Gy), respectively. Films should be handled with care and never touched with bare hands to avoid uncertainties.

The size of the full GAFchromic film is 20 cm x 25 cm and this can be cut into desired sizes. This feature of radiochromic films and their high spatial resolution make them a good choice for small field dosimetry.

After irradiation, pixel values of the films can be read out with a special flatbed scanner and software. With a calibration curve, pixel values can be transformed to optical density then converted to the dose. The calibration curve for every film batch with the same lot number is performed in reference conditions [22, 23].

1.6 Proton Treatment Planning

The treatment planning process consists of several steps which are described in the following subsections [5, 14].

1.6.1 Imaging

Imaging serves as the initial stage in the treatment procedure. Imaging for radiotherapy which is used for treatment planning is different compared to the other types of imaging like diagnosis imaging. In this type of imaging, the acquired data are crucial for patient positioning and the generation of treatment plans. The position of the patient should be the same as the position during irradiation treatment. The respective images have to be imported into the treatment planning system.

1.6.2 Target Contouring and Treatment Plan Creation

The next steps are defining and delineation of the target and organs at risk. All of the configurations and structures must be described in treatment plans. Depending on the location of the target the organs at risk (OARs) are the heart, brain, skin, lung, glands, bones, spinal cord, liver, nerve and vessels.

During target contouring, several factors such as irradiation mode, prescribed dose, treatment technique and machine had to be established.

1.6.3 Dose Calculations and Optimization

Dose calculation is a crucial step in the treatment planning process. Dose calculation aims to predict the delivered dose to the target volume and the surrounding tissue. The information about the geometry of the treatment table, patient, treatment field size and energy and information about the density of the target is required for dose calculation.

There are different algorithms for dose calculation. Two main methods in particle therapy are pencil beam (PB) and Monte Carlo (MC) approaches.

Pencil Beam

Pencil beam mode is one of the most used approaches for calculating proton dose. There are many different pencil beam algorithms, the first algorithm was designed for passive beam scattering. The main idea of all analytical algorithms is the infinite division of pencil beams that passes through a certain field. The single doses are affected by scattering and energy loss in the pass through material (traversed) The total dose distribution is equal to the integral over the convolutions of proton fluence and pencil beam dose kernel for all single pencil beams: $\int (fluence * kernel)$ [14], [22–24].

Monte Carlo

Monte Carlo is one of the most accurate and realistic approaches in dose calculation. It includes primary and secondary ions, tissue inhomogeneities, multiple scattering and nuclear interactions. The disadvantage of this method are time-consuming calculations, which can only be reduced by reducing accuracy [5, 22].

The objective of the optimization is to manually adapt the parameters in the treatment plan to find a balance between target coverage with the prescribed dose and protecting the surrounding tissue and organs at risk. There are several optimization approaches: Each field in the plans is separately optimized to provide a homogeneous target coverage in Single Field Uniform Dose (SFUD) delivery. In Multiple Field Uniform Dose (MFUD) delivery, all fields are optimized together. PBS can be delivered by most of the modern proton therapy treatment systems [25].

Disadvantages of the PBS technique are the costs, and for site treatments with organ movements, it needs a high accuracy patient positioning [14].

1.7 MedAustron

MedAustron is a center for ion therapy and research that is located in Wiener Neustadt in Lower Austria, 50 km south of the Austrian capital city Vienna. Proton radiation therapy and a relatively rare type of particle radiation therapy using carbon ions are available at MedAustron. The start of construction was in March 2011 and patients are treated since 2016 with protons and since 2019 with carbon ions. MedAustron provides

besides the patient treatment, research possibilities for universities and different institutions.

The main core of MedAustron is a synchrotron accelerator, which provides accelerated protons and carbon ions with ranges up to 38 cm in water. The therapeutic energy for particles for protons is ranging from 62.4 MeV to 252.7 MeV, while for carbon ions from 120 MeV/n to 402.8 MeV/n. Protons with energies up to 800 MeV can be used for research purposes.

Before accelerating the protons in a synchrotron, a linear accelerator, which speeds up the protons up to 7 MeV, is used as a pre-accelerator [26]. Then protons are injected and circulated into a narrow vacuum tube ring with the aid of bending magnets located around the circular path of the beam.

There are two types of magnets: The dipole and quadrupole. Dipole magnets keep the beam on a circular path, the quadrupole is responsible for the focus of the beam [15].

Protons are accelerated in radiofrequency cavities powered by sinusoidal voltage with a frequency that is equal to the frequency of circulating protons [26]. Once the energy of proton beams gets the desired energy, the proton beams leave the synchrotron. Figure 1-5 depicts a schematic diagram of a synchrotron accelerator.
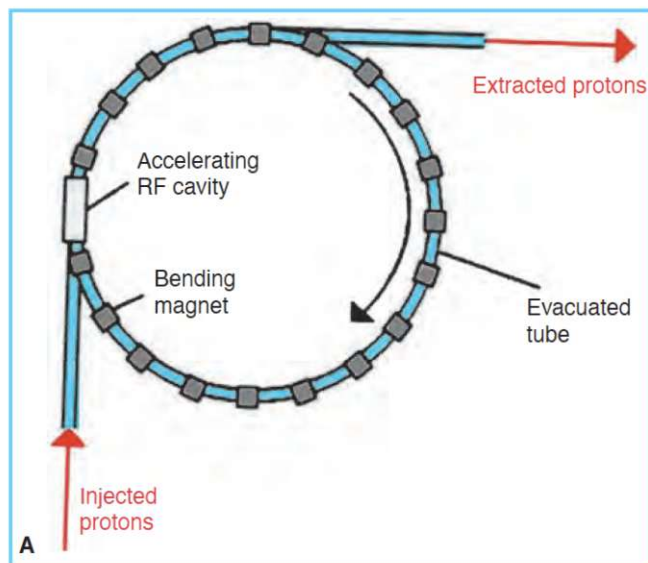
Figure 1-5: Schematic diagram of proton acceleration in a synchrotron. Synchrotrons produce the beams at any desired depth by accelerating protons to precise energies.

For beam delivery, MedAustron employs the pencil beam scanning (PBS) technique. In PBS a small beam spot is steered to a dedicated place by powerful magnets and scanned throughout the whole treatment area. It supports all dose delivery patterns and depth-dose modulations [14].

The intensity of each spot can be adjusted. Also by varying energies, different depths can be achieved. Several spots which are divided over the various fields, are combined to achieve the dose coverage of the target.

MedAustron has four irradiation rooms, three of which are reserved for medical care and patient treatment. The fourth room is experimental, where the beam can be used for research purposes in a dedicated irradiation room. All of the four rooms are shown in Figure 1-6.

- IR1: fixed horizontal beam (non-clinical research)
- IR2: fixed horizontal and fixed vertical beam
- IR3: fixed horizontal beam
- IR4: proton gantry (nozzle can be moved around the patient and enable treatment from each angle.)

Each of the rooms is equipped with a robotic system that is used for patient positioning and an imaging ring for accurate positioning purposes. All measurements reported in this thesis were completed in IR1 (non-clinical research).
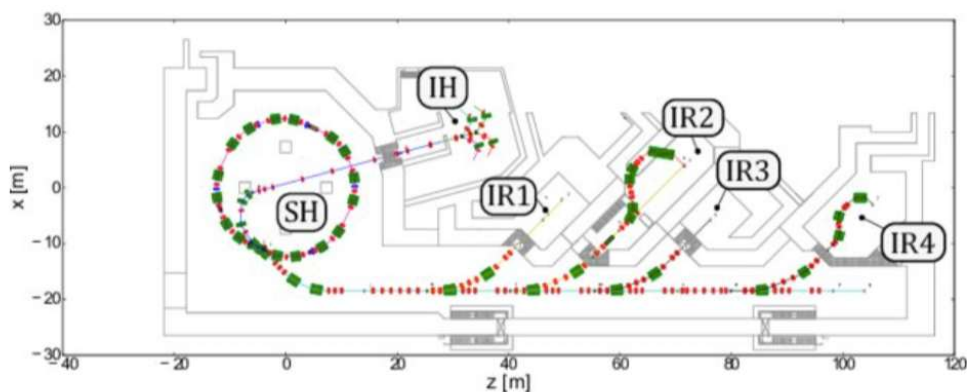
Figure 1-6: Accelerator layout of MedAustron facility, Synchrotron Hall (SH), Injector Hall (IH) and four irradiation rooms IR1-IR4 [27]

1.8 Motivation

Pre-clinical in-vivo research with animal models has a high potential to help understanding and improving the effect of particle interactions with tissues during radiation therapy. This type of research using small animals is the next step moving from in-vitro experiments (performed with cells) toward the implementation of the knowledge into clinical practice [28]. Mouse models are applied to understand the genetic basis of tumors, the development of cancer, the effect of radiotherapy and the response of radiotherapy on cells, tissue and whole organs [29]. In radiotherapy, it is important to observe not only the response of the tumor but also the response of the surrounding healthy tissues and OARs to irradiation.

Small field proton therapy is an evolving field and has certain concerns that must be tackled. Beam's transverse profile has a wider penumbra [30]. Beams are relatively large compared to the target size in small animals. In order to confine the irradiation beams and spare the surrounding tissue a collimator have to be used. In addition, the target is positioned at a shallow depth. Accordingly, a pre-absorber should be used to pull the Bragg peak to the surface. These challenges are present at the treatment planning stage as well as in the dose delivery.

Due to the small structures in the small animals, the beam line for the irradiation of small fields with proton beams has to be adapted, modified and thoroughly tested. The aim of this thesis was to irradiate small fields relevant to small animal irradiation with proton beams and to investigate the application and limitation of regular equipment designed for patient treatments when utilized for in-vivo experiments.

Therefore, experiments with phantoms with different target sizes in different setups using various external elements in the beam path like collimator and pre-absorber were performed. The results were evaluated in order to investigate if and how the different elements influence the dose distribution in the target. Another purpose was to investigate if the current using TPS is suitable for small targets. Hence, treatment plans were created for small targets with a diameter of 1.2 cm and 0.8 cm. The prescribed dose was compared to the predicted dose from TPS and measured dose for various setups. A combination of active and passive detectors was used for dose determination and validation in small field irradiation.

Chapter 2

Materials and Methods

This chapter describes the materials and methods, which have been used for this thesis project. Firstly, the treatment planning system, which was used to generate the treatment plans is explained. Moreover, the configuration of the phantom and the small target and the overall used materials will be discussed in detail. Then the external elements which were placed in the beam pathway are described. Besides, the different irradiation scenarios performed were investigated. Finally, the used detectors, which were suitable for small field irradiation were analyzed. The investigated approaches for data evaluation will be presented as well.

2.1 Treatment Planning System

For dose calculation, computed tomography scans of the phantom were acquired then the scans were imported into the Treatment Planning System (TPS-Raystation, Raysearch, Sweden). In in-silico studies by importing the CT images into the treatment planning system the location of the region of interest (ROI) and other structures can be determined. The treatment plans can be created and optimized to ensure the optimal target coverage while sparing healthy tissue around the target as much as possible.

The cylindrically shaped targets, with different diameters, were delineated on the CT scan of the phantom in the TPS. The targets were defined as ROI. The prescribed dose was 1 Gy in all of the cases (RBE). The length of the target was 1.5 cm in all of the cases, but the diameter varied from 0.8 to 1.2 cm.

During the treatment plan creation some parameters had to be defined, e.g. treatment technique, treatment machine, number of fractions, treatment modality and prescribed, minimum and maximum dose.

The generated plans, including the information about the gap between the phantom and the nozzle, the usage of range shifter or bolus, among other details, are given in Table 2-1. Table 2-2 lists the common parameters between all of the cases. The dose for proton beams was calculated by means of a Monte Carlo algorithm.

Table 2-1: Plans for various setups.

Plans	Pre-absorber	Airgap	Aperture	Target diameter
12T-isoAG-RS-15cmAp	RaShi	Iso-center	1.5 cm	1.2 cm
08T-isoAG-RS-11cmAp	RaShi	Iso-center	1.1 cm	0.8 cm
08T-isoAG-B-11cmAp	Bolus	Iso-center	1.1 cm	0.8 cm
08T-isoAG-RS-1cmAp	RaShi	Iso-center	1 cm	0.8 cm
08T-isoAG-RS-noAp	RaShi	Iso-center	Non	0.8 cm
08T-10AG-RS-noAp	RaShi	10 cm	Non	0.8 cm

Table 2-2: Settings in TPS.

Parameter	
Treatment technique	Pencil Beam Scanning
Treatment machine	IR1HBL
Number of fractions	1
Treatment modality	Protons
Prescribed Target dose	1 Gy
Beam direction	Horizontal

The imported CT scans of the phantom with delineated target and 4 positions for the detectors are indicated in Figure 2-1. Figure 2-2 shows some samples of the created treatment plans and their corresponding dose distributions calculated by the TPS.
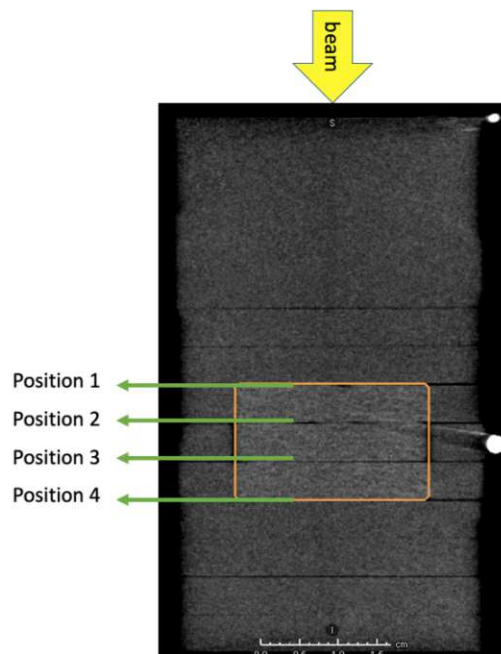
Figure 2-1: Imported CT scan of the phantom to the treatment planning system. Detectors were placed at positions 1,2,3 and 4 as indicated. The beam was coming from the top.
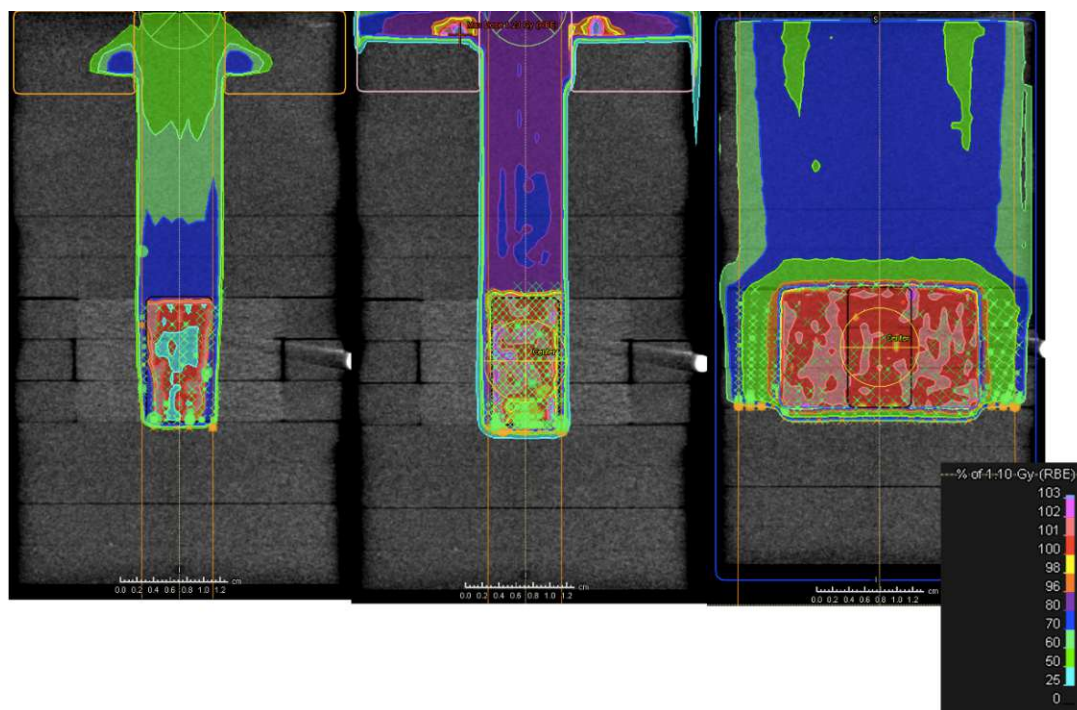
Figure 2-2: Examples of TPS plans and the corresponding dose distributions

2.2 Phantom

The used phantom was composed of a $4\times4\times0.5$ cm^3 polymethylmethacrylate (PMMA) plates. A cylindrically shaped water equivalent material 2.5 cm in diameter, was surrounded by PMMA material. The PMMA has a density of 1.18 g/cm^3. The material in the center of PMMA, which represented the target, has a density of 1.04 g/cm^3 and was made of tissue equivalent material from Gammex company. The phantom was formed by four layers of plates. The first layer was a pure PMMA plate and the other three layers consisted of water equivalent 'Gammex' material in the center.

Figure 2-3 depicts the phantom used in this master thesis. The phantom was designed to be used with detectors between the individual plates.
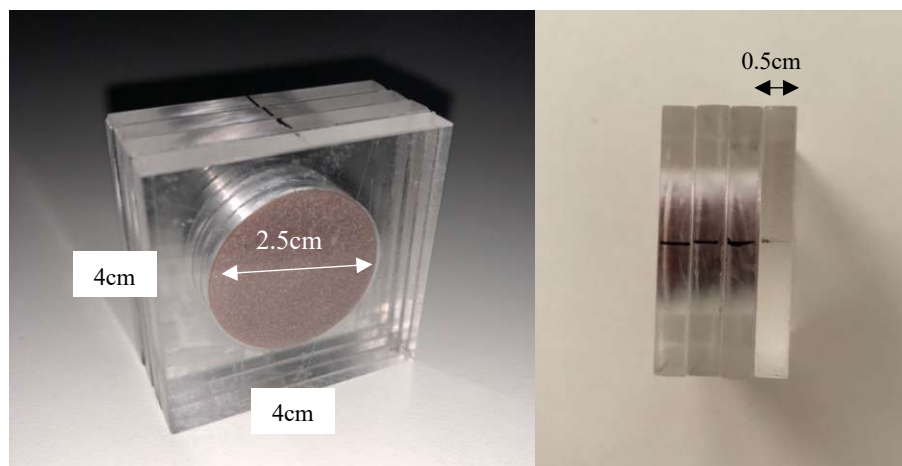
Figure 2-3: The phantom made of PMMA material with water equivalent material insert representing the target

As shown in Figure 2-4, the detectors were placed in four positions within the phantom, to investigate the dose distribution inside and around the small target area.

Figure 2-4: EBT3 films inserted at different depths of the phantom

2.3 Setup for Irradiation

To investigate the effect of irradiation on the small targets with proton beams, different setups were tested. Different beam shape devices formed different setups for irradiation, e.g. various target sizes, pre-absorbers and different aperture sizes. In each setup, the dose distribution inside the respective targets was measured with the detectors.

As shown in Figure 2-5, the beam from the accelerator passes through the nozzle on the left side and then through different beam shape devices to the target and detectors on the right side, respectively. Each scheme is dedicated to one measurement position (for detectors) in the target. The phantom was positioned on the irradiation couch at 10 cm and 66.1 cm (iso-center) away from the nozzle, also labeled as an airgap.
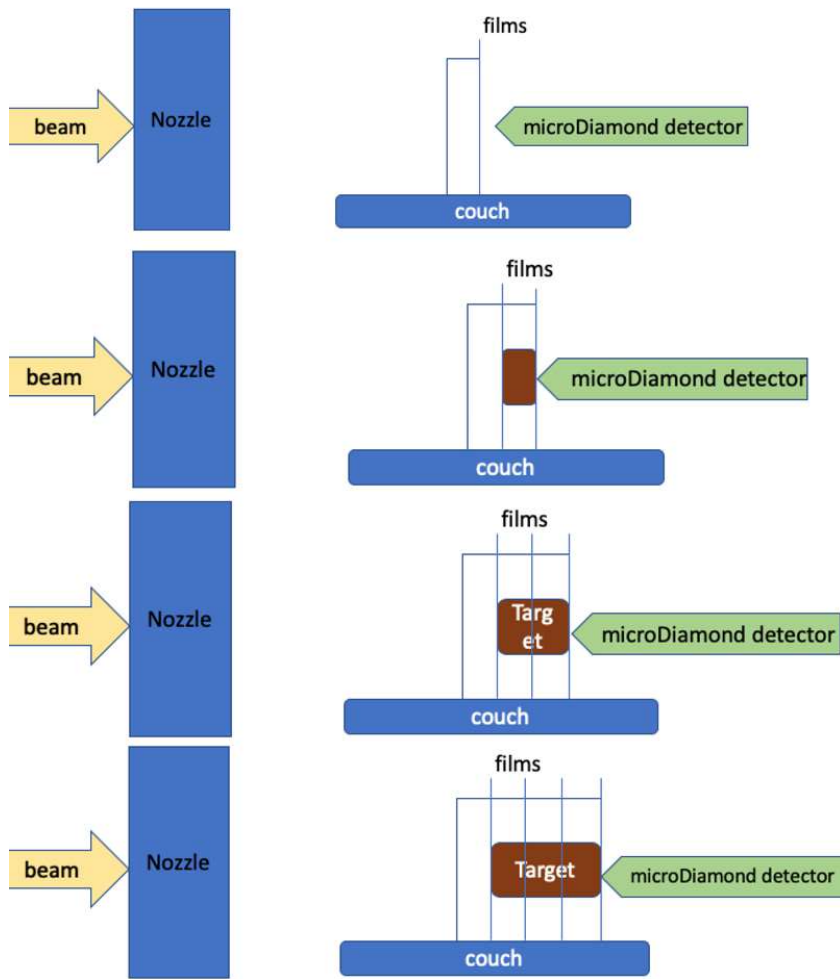
Figure 2-5: General setup for measurements

2.3.1 Pre-absorber

The available energy range of proton beams for treatment at MedAustron is between 60 MeV and 250 MeV, which is equivalent to a depth of 3 cm and 38 cm. Even the minimal available energy limits the irradiation to a few centimeters. To treat superficial tumors located at depth shallower than 3 cm, the presence of a pre-absorber is essential to modify the penetration depth. This additional material decreases the energy and hence the penetration depth of the beam in tissue. Pre-absorbers can either be range shifters, which are included in the nozzle, or bolus placed in front of the phantom.

Range Shifter

The range shifter is one of the components located in the nozzle. It can be moved in and out of the beam pathway automatically according to the generated treatment plan. The range shifter at MedAustron is made of a 3 cm thick PMMA. Figure 2-6 depicts the MedAustron nozzle components.
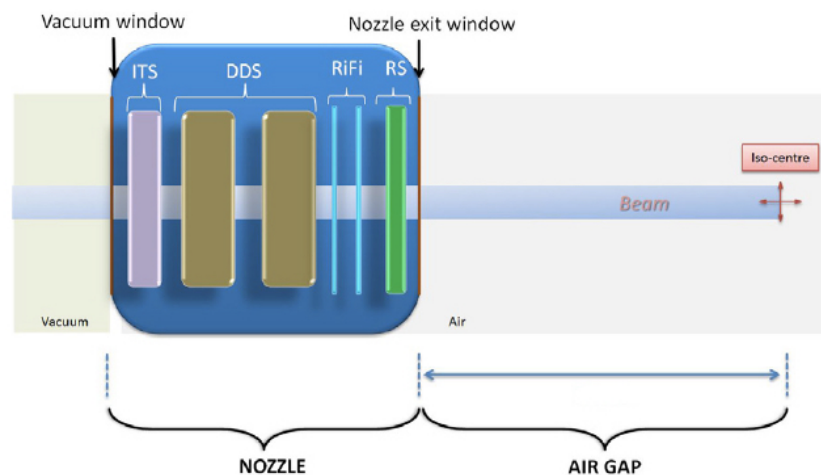
Figure 2-6: Schematic illustration of the MedAustron nozzle. It contains a vacuum window, independent termination system (ITS) box, dose delivery system (DDS) boxes, ripple filter (RiFi) slots (78 and 80 cm from the iso-center are relevant only for carbon ions) and range shifter (RS) slot (73 cm from the iso-center) [31]

Bolus

A bolus, as used for clinical treatments, is a tissue equivalent material, made of e.g. paraffin wax, Lucite, PMMA, Superstuff or Superflab, and placed generally in front of the patient to reduce the penetration depth [26].

In the measurements for modulation of the penetration depth, a PMMA bolus with a thickness of 2 cm was placed directly in front of the phantom. Figure 2-7 shows the used bolus in this thesis.
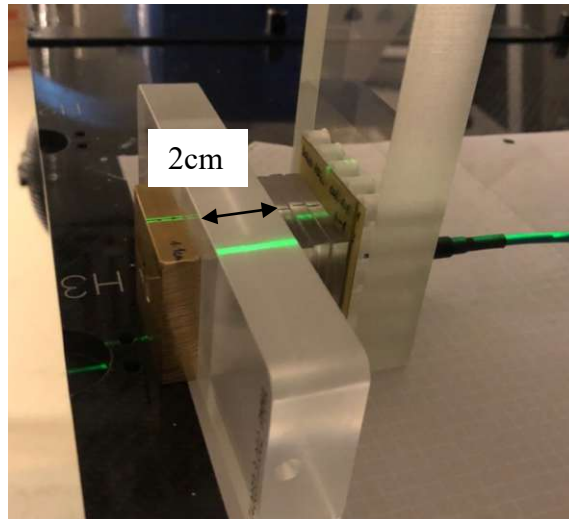
Figure 2-7: 2 cm PMMA bolus

2.3.2 Aperture

The main function of the aperture is to confine the radiation dose to the target, by shaping the proton beam into the target shape and limiting the dose out of its area. The aperture was placed in front of the target in such a manner that the center of the target, as well as the center of the aperture, was aligned with the beam.

The employed apertures in the measurements were made of brass with the composition of copper (Cu) and zinc (Zn) alloy and the density of 8.4 g/cm^3 [32]. In the current study, a square-shaped plate with a thickness of 1cm was used with a cylindrical aperture and different opening radii: 1.5 cm, 1.1 cm and 1 cm. Throughout the thesis, the term aperture was used instead of the term collimator.

Figure 2-8 shows the brass apertures used in the measurements.
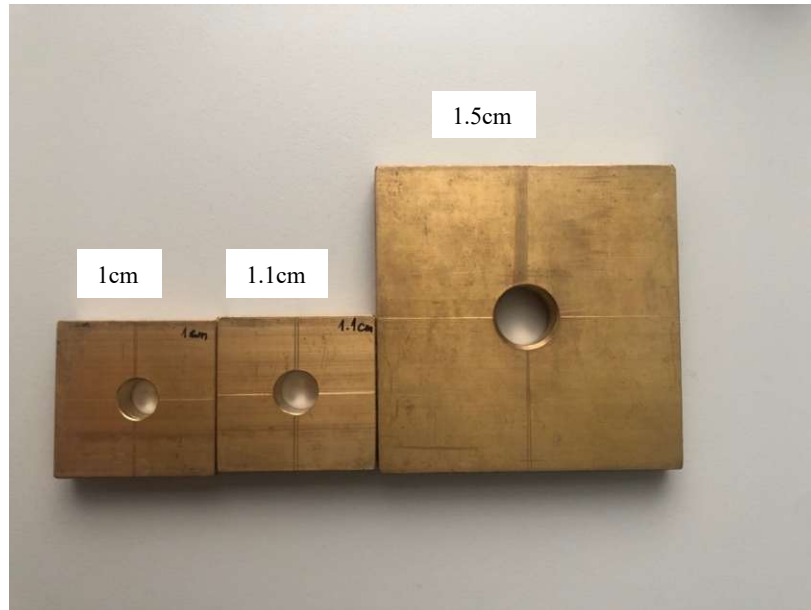
Figure 2-8: Apertures

2.4 Setup Scenarios

In this subsection, the setup scenarios will be discussed in detail. It has to be noted that for each of the subsequent cases 12 films were irradiated at four different depths in SOBP. These 12 films were separated into four sets between phantom layers and each set contained three films unless otherwise indicated.

The CT scan of the phantom was imported to TPS, the target was delineated and the treatment plans were generated.

2.4.1 Comparison of the Dose Distribution with and without an Aperture

To compare the dose distribution in the target with and without an aperture two plans were delineated in the TPS, the dose was calculated with and without an aperture, and finally the setups were prepared and irradiated.

Setup A contained no aperture. In Setup B a brass made aperture with an opening of 1.1 cm was overwritten on the CT scan. The distance between the aperture and phantom was overwritten in TPS with air. The range shifter was applied, in both of the setups.

The energy range in both of the setups was from 72.40 MeV to 88 MeV. Figure 2-9 shows the CT scan of the phantom with the corresponding delineation and Figure 2-10 illustrates a schematic overview of the two mentioned setups. Table 2-3 lists the details of the two setups.
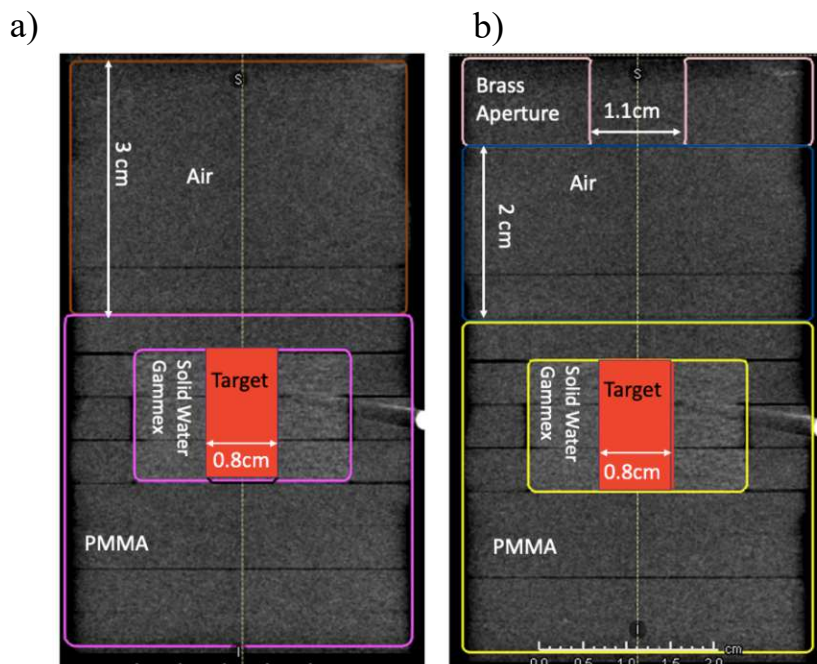
Figure 2-9: Structure delineation and material overwrite in Setup A(a) and B (b)

a)

b)
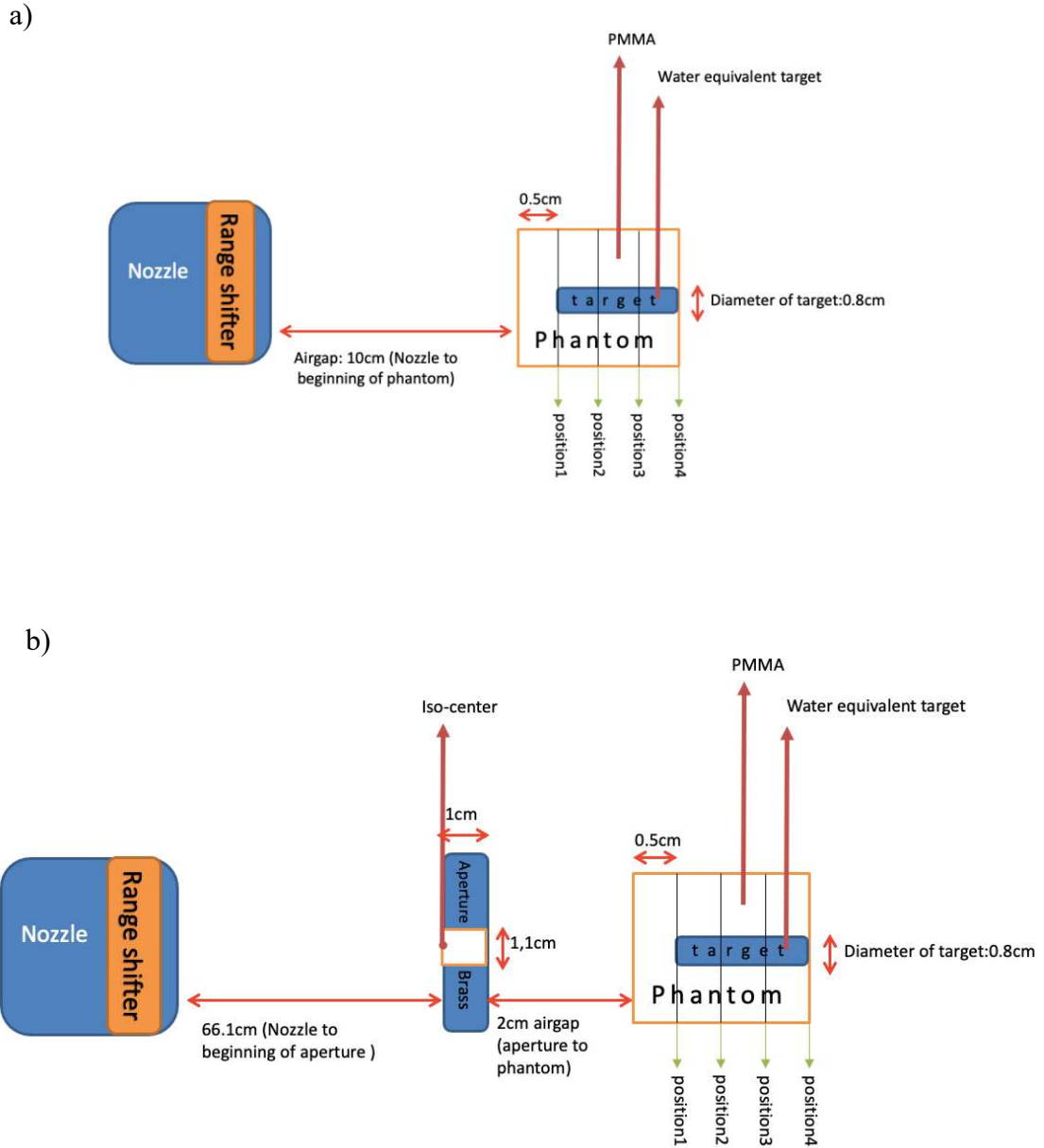
Figure 2-10: Schematic overview of two setups, without (a) and with (b) aperture

Table 2-3: Setup A and B in detail

	Setup A	Setup B
Target diameter	0.8 cm	0.8 cm
Pre-absorber	Range shifter	Range shifter
Airgap	10 cm	Iso-center
Aperture	**non**	**1.1 cm**

2.4.2 Limitation of Aperture Size

To determine the smallest possible aperture relative to the target size, two different aperture sizes were tested.

In the TPS the brass made apertures with the opening size of 1.1 cm and 1 cm were delineated for the Setup C and D, respectively. The distance between the aperture and the phantom was overwritten with air since the range shifter was inserted. The energy range of both setups was from 71.40 MeV to 87 MeV.

Figure 2-11 shows the structure delineation and material overwrite in TPS with the corresponding components. Table 2-4 shows the detail of the two cases.
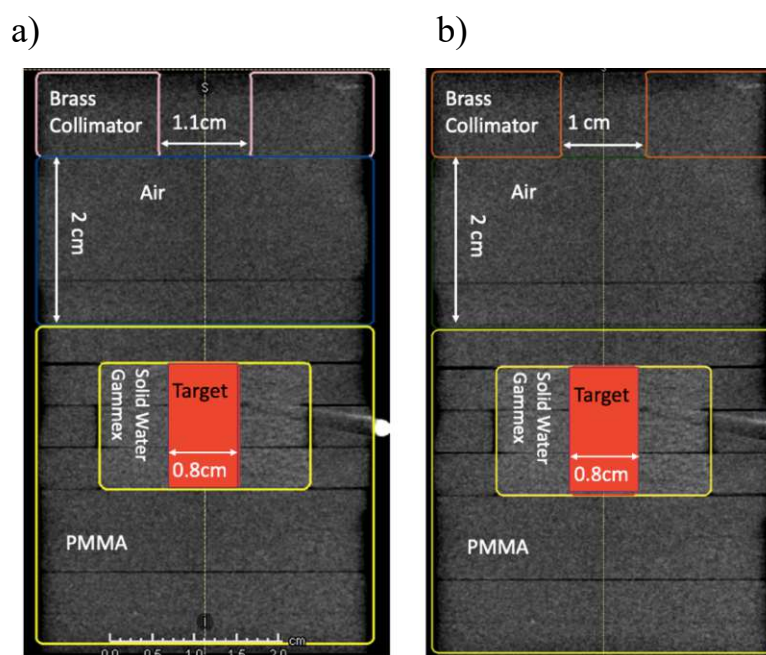
Figure 2-11: Delineation of the components in Setup C (a) and D (b).

Table 2-4: Details for aperture size study:

	Setup C	Setup D
Target diameter	0.8 cm	0.8 cm
Pre-absorber	Range shifter	Range shifter
Airgap	Iso-center	Iso-center
Aperture	**1.1 cm**	**1 cm**

2.4.3 Comparison of Different Pre-absorbers and Different Target Sizes

The purpose of the following analysis was to investigate the role of different pre-absorbers on dose distribution in small targets. In addition, due to the small field irradiation restrictions of TPS, the least feasible size of the target, for which acceptable results can be achieved, was investigated.

Different Pre-absorbers

The pre-absorbers are necessary for irradiation of shallow targets that are close to the surface. The lowest energy available at MedAustron is 62.4 MeV. The application of a pre-absorber causes energy reduction, which pulls the Bragg peak more to the surface. Two types of pre-absorber were compared in this thesis: Bolus (2 cm PMMA) and range shifter. To investigate the impact of the mentioned pre-absorbers on dose distribution in the small targets, treatment plans with different pre-absorbers were delineated in TPS, the dose was calculated and then the setups were irradiated.

The bolus, placed directly in front of the target, was overwritten with PMMA in TPS: Setup E (Figure 2-12 a). The range shifter was inserted into the nozzle: Setup F (Figure 2-12 b). The distance between the aperture and the nozzle was 66.1 cm (iso-center). The energy range of Setup E was from 62.40 MeV to 76.90 MeV while in Setup F was from 71.40 MeV to 87.20 MeV. Figure 2-13 depicts the delineation of components in the TPS. Table 2-5 provides the details of cases.

b)
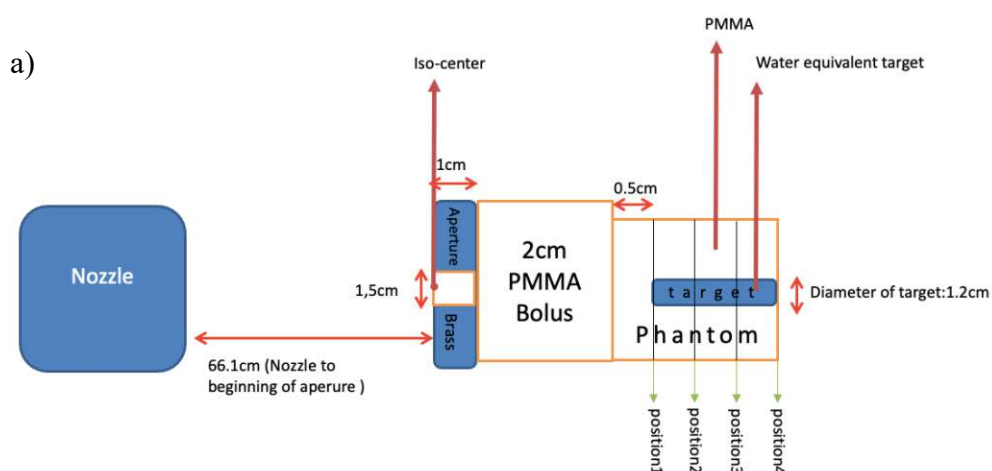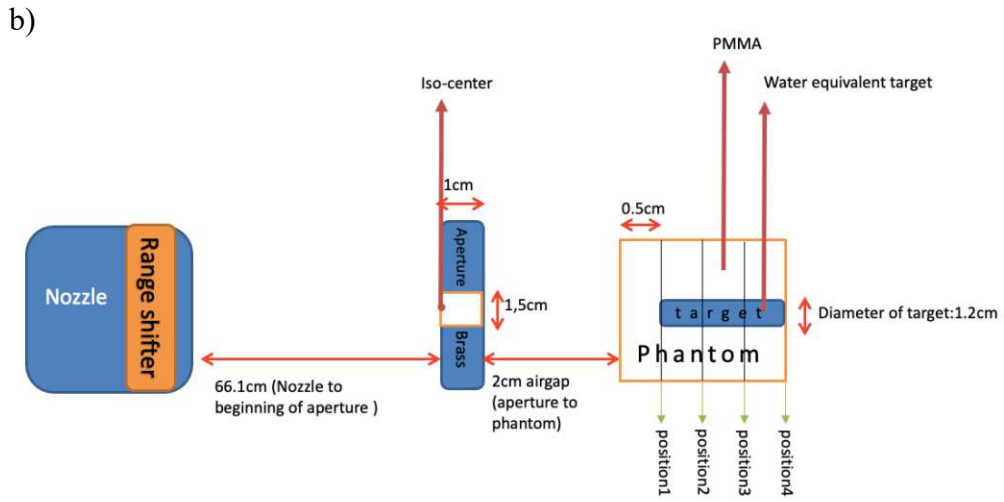
Figure 2-12: Illustration of two cases with bolus (a) and with range shifter (b)
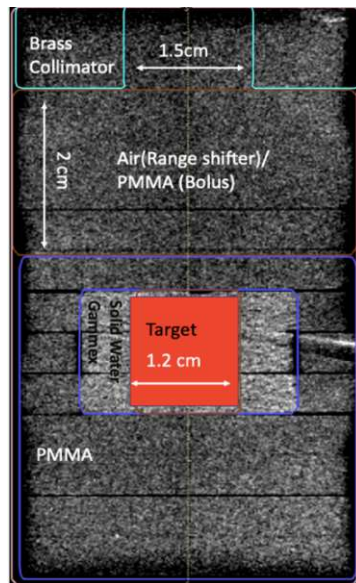
Figure 2-13: Delineation of structures in TPS in Setup E (2cm PMMA as bolus) and Setup F (2cm air since range shifter was in)

Table 2-5: Details for pre-absorber type study:

	Setup E	Setup F
Target diameter	1.2 cm	1.2 cm
Pre-absorber	**Bolus**	**Range shifter**
Airgap	Iso-center	Iso-center
Aperture	1.5 cm	1.5 cm

Different Target Sizes

Relevant target volumes in small animals can vary between ca. 2 cm^3 down to 0.5 cm^3. The TPS is not recommended for irradiation of volumes smaller than 2 cm^3. To investigate its limitations, different target sizes were delineated in TPS, the dose was calculated and the treatment plans were irradiated. Then the dose distributions were compared. The energy range of Setup G and H was from 71.40 MeV to 87.20 MeV.

Figure 2-14 shows the delineation of the components in TPS. The details of the two setups are given in Table 2-6.
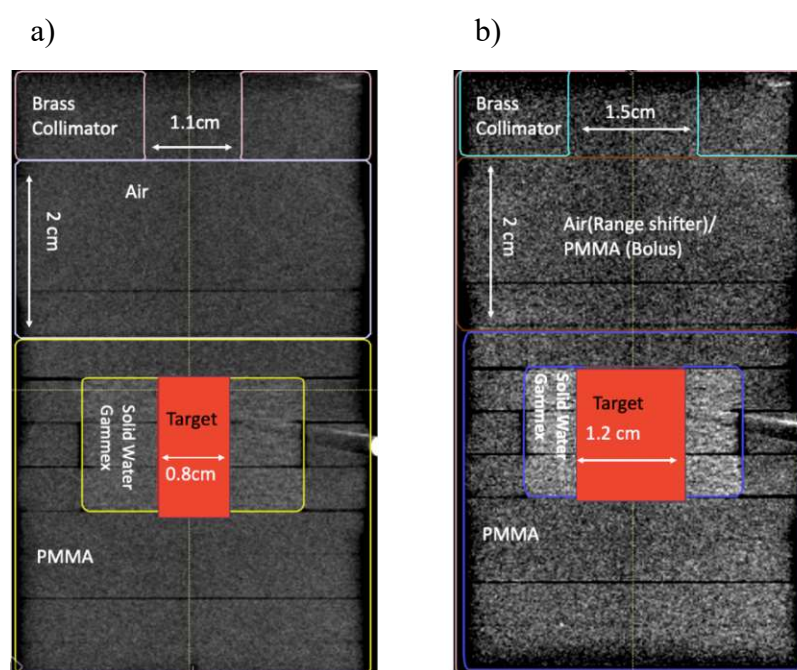
Figure 2-14: Delineation of the Setup G (a) and H (b)

Table 2-6: Details for irradiation of targets with different sizes:

	Setup G	Setup H
Target diameter	**0.8 cm**	**1.2 cm**
Pre-absorber	Range shifter	Range shifter
Airgap	Iso-center	Iso-center
Aperture	1.1 cm	1.5 cm

2.4.4 Positioning Accuracy of the Aperture

To test the positioning accuracy of the aperture in the setup and the impact of the positioning on dose distribution in the target, several positions of the aperture were tested. Aperture was 'misplaced' laterally to the respect of the target.

Lateral Shifts

With this setup, the same treatment plan was delineated and irradiated as in Setup C. The measurements were performed with a 1.1 cm aperture at five different positions: at the center of the target; 1 mm right of the target; 1 mm left of the target; 2 mm right of the target and 2 mm left of the target. For each setup, four films were irradiated at four different depths 5mm, 10mm, 15mm and 20mm of the target, with energies ranging from 74.20 MeV to 87.20 MeV. All four films were irradiated at the same time.

The range shifter was used as a pre-absorber for both of the approaches and the aperture was placed on iso-center. Figure 2-15 depicts the configuration of this setup. Table 2-7 lists the details of the mentioned setups.
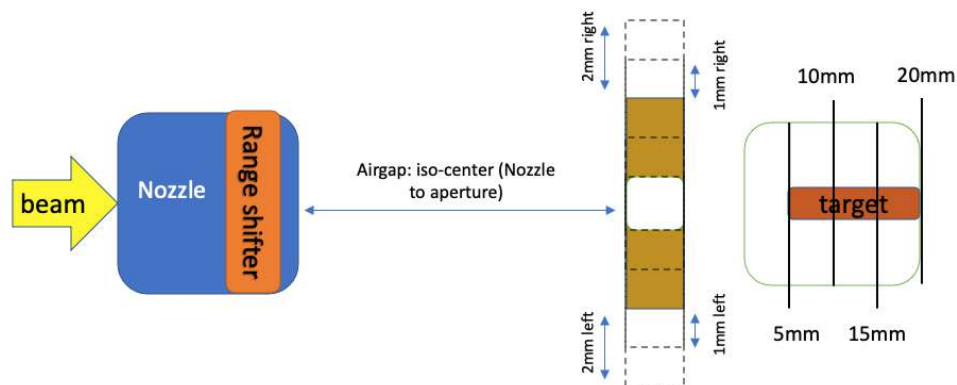
Figure 2-15: Schematic layout of irradiation setup with the shifting aperture laterally

Table 2-7: Details of lateral 'misplacement' of the aperture

	Setup I	Setup J	Setup K	Setup L	Setup M
Target diameter	0.8 cm	0.8 cm	0.8 cm	0.8 cm	0.8 cm
Pre-absorber	RaShi	RaShi	RaShi	RaShi	RaShi
Airgap	Iso-center	Iso-center	Iso-center	Iso-center	Iso-center
Aperture	1.1 cm	1.1 cm	1.1 cm	1.1 cm	1.1 cm
Position of aperture	Center	1mm Right	1mm Left	2mm Right	2mm Left

2.4.5 Aperture not modeled in TPS

In this approach a setup was tested with an aperture, however, the aperture was not considered in TPS. A treatment plan for a setup without the aperture was designed and irradiated as shown in Figure 2-9 (a). An aperture was simply placed in front of the setup.

The distance between the phantom and the nozzle was 66.1 cm (iso-center) and an aperture with an opening size of 1.1 cm was placed in front of the phantom (see Figure 2-16). The energy range was from 72.40 MeV to 87.20 MeV. Table 2-8 lists the details of the setup.
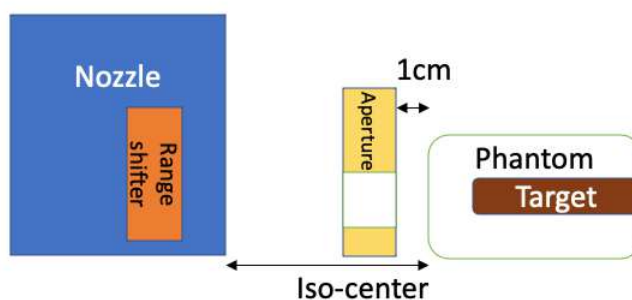
Figure 2-16: Schematic layout of the placement of an aperture in front of the phantom without considering it in TPS

Table 2-8: Details of Setup N

	Setup N
Target diameter	0.8 cm
Pre-absorber	Range shifter
Airgap	Iso-center
Aperture	1.1 cm

2.5 Small Field Dosimetry

The delivered doses and the dose distributions were acquired in the target with radiochromic EBT3 films in combination with a microDiamond detector. The two detector types complemented each other. The EBT3 film is a passive type of detector suitable for dose distribution as well as absolute dosimetry. MicroDiamond detector is an active detector with very small active volume which can be applied for absolute dosimetry.

2.5.1 EBT3 Films

EBT3 films from GAFchromic (Ashland, NJ, USA) are radiochromic dosimeters and are commonly used in radiation dosimetry due to their high spatial resolution, multiple readouts, storage of results and adjustable size [33]. They are capable of measuring the dose delivered in two dimensions and can be used for both relative and absolute dosimetry. EBT3 films are used in external beam radiotherapy, radiosurgery and brachytherapy. Unlike other film types, EBT3 films do not require a darkroom, chemical processing, or post-exposure processing. EBT3 films are optimized for doses ranging from 0.2 to 10 Gy with the red color channel, making them suitable for use in radiation therapy. They consist of 27μm thick active layer, containing active component, marker dye and stabilizers. The active layer is between two 120 μm thick transparent substrates.

EBT3 films can be handled in ambient light but should be stored away from radiation sources at dark sites. Since these films are water-resistant, they can be immersed in water phantoms. An economic flatbed color scanner is required to read the irradiated films.

A disadvantage of radiochromic films is their nonlinear response at higher doses. Furthermore, it is necessary to wait up to 48 hours after exposure to provide full-color development [34].

Film Scanning, Irradiation and Calibration

In this thesis, all of the EBT3 films (lot number: 03122003) were cut into 4cm × 5cm pieces. Twelve films were used for each setup where three films were placed at each measurement position. For film evaluation of irradiated films as well as background, an EPSON Expression 11000XL flatbed scanner was used. It is recommended to scan the irradiated films 24 to 48 hours after irradiation. The Epson scanner should be warmed up before the scanning. Films were placed at the center of the scanner and scans were saved in TIF (*.tif) format. They were scanned once before the irradiation for the background acquisition and three times after the irradiation. Only the red channel of the scanned images in TIF format was analyzed.

The optical density (OD) of the films was calculated from the mean of pixel values (PV) of the background and irradiated films as following:

$$OD_{red} = log_{10}\frac{PV_{Bg}}{PV_{Irr}} \qquad\qquad (2-1)$$

where PV_{bg} and PV_{irr} are the averages of background and irradiated pixel values [35].

The dependency of optical density and dose can be described as the 4th degree polynomial, which is known as the calibration curve (Equation 2-2). A calibration curve for the films with the mentioned lot number, was created in October 2020 in the frame of a different project.

$$Dose = a.OD^4 + b.OD^3 + c.OD^2 + d.OD^1 + e \qquad\qquad (2-2)$$

where

OD = optical density	c = 0.1063
a = -0.0375	d = 0.2950
b = 1.0114	e = -0.0000

The calibration curve was created for doses up to 12 Gy.

Figure 2-17 shows the EBT3 film composition, the EPSON scanner and a sample of EBT3 film scanned for background and after irradiation.
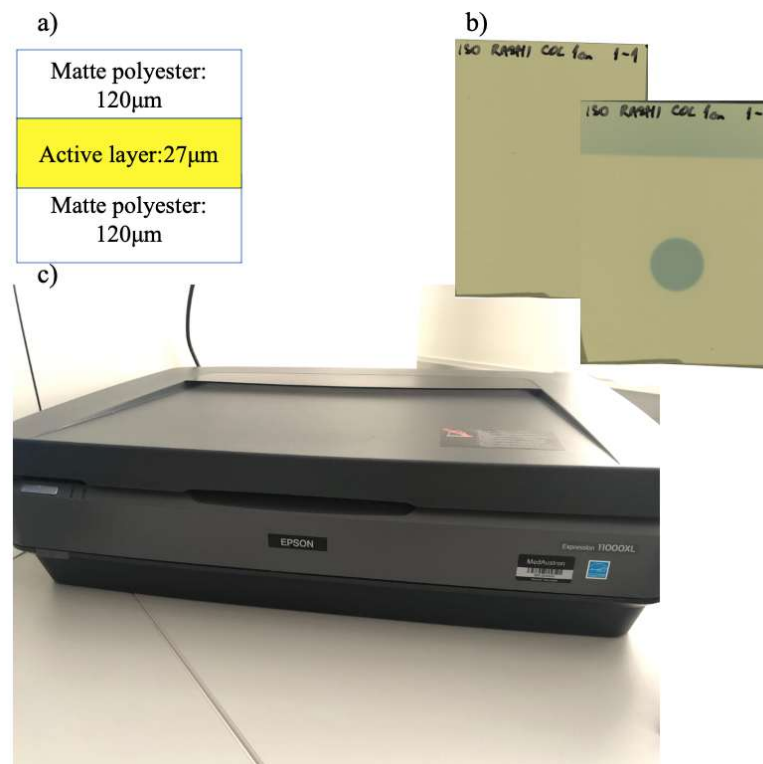
Figure 2-17: Composition of EBT3 a film (a), background and irradiated film (b), EPSON Expression 11000XL flatbed scanner (c)

Film Analysis

All film scans were evaluated in MATLAB (MathWorks Inc., USA, Version R2015b). The area for evaluation of the exposed part of the films was chosen manually as illustrated in Figure 2-18. The same area was chosen from the background scans. The average of pixel values in the region of interest and the background films over three scans were calculated and used for further evaluation. The area of 2 mm × 2 mm at the center of the target (Figure 2-18 (b)) represented the pixels which were evaluated for the absolute dose determination.

The optical density was calculated by equation (2-1) and it is converted to the dose through equation (2-2).

Figure 2-18 depicts the region of interest in the films.
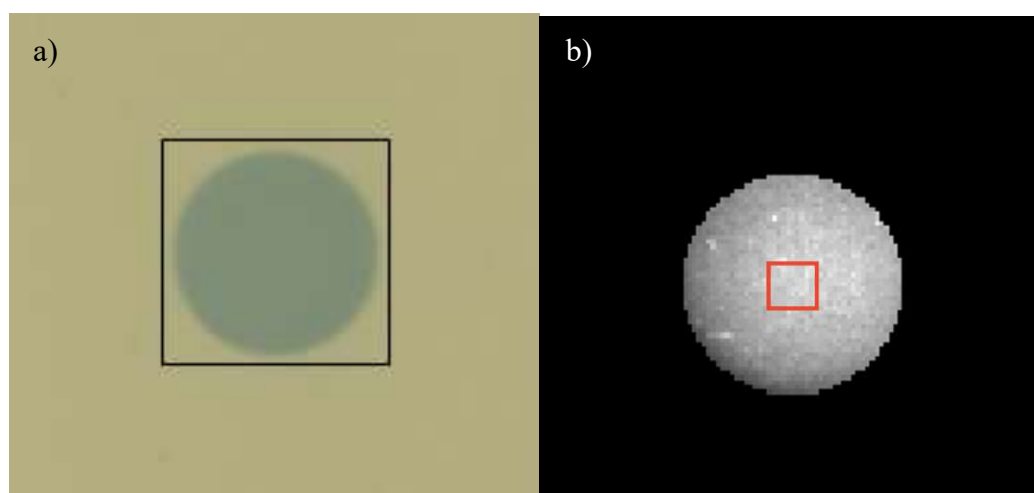
Figure 2-18: (a) selected area in the film which was evaluated for the background and irradiated film, (b) evaluated area in the center of the target for absolute dose determination

2.5.2 MicroDiamond Detector

In addition to EBT3 films, the microDiamond detector (Type 60019 SN 122208, PTW-Freiburg, Germany) was used for absolute dosimetry. It had a circular radius of 1.1 mm with an active volume of 0.004 mm^3 and thickness of 1 μm. The small active volume assures suitability of detector for small field dosimetry. It was applied in face in orientation. In front of the active volume a material of 1mm WET (water equivalent thickness) is mounting.

The technical instructions for the microDiamond detector recommend the bias voltage of 0 V and a pre-irradiation dose of 5 Gy [20].

Prior to measurements the cross calibration of the microDiamond detector was performed in a stationary water phantom MP1 (PTW, Freiburg) against the reference chamber (e.g. Farmer chamber) in terms of absorbed dose to water in the beam quality Q_{cross}:

$$N_{D,W,Q_{cross}}^{cross} = \frac{M_{Q_{cross}}^{ref}}{M_{Q_{cross}}^{cross}} \times N_{D,W,Q_0}^{ref} \times K_{Q_{cross},Q_0}^{ref} \qquad (2-3)$$

$M_{Q_{cross}}^{ref}$ and $M_{Q_{cross}}^{cross}$ are a reference and microDiamond detector dosimeter readings respectively corrected for temperature and pressure, electrometer calibration, polarization and ion recombination effects. N_{D,W,Q_0}^{ref} is the calibration factor for reference chamber obtained at ^{60}Co and K_{Q_{cross},Q_0}^{ref} was the beam quality correction factor for the reference chamber [36].

To measure the collected charge and supply the detector with the needed voltage PTW Unidos webline electrometer, with the serial number 000883 was used. Figure 2-19 shows the microDiamond detector and the electrometer that were used for data acquisition.

The measured current from the electrometer is converted to dose with the following expression:

$$Dose_{Diamond\ detector}\ [Gy] = M_{Diamond\ detector} \times K_{Diamond\ detector}^{ref} \qquad (2-4)$$

$M_{Diamond\ detector}$ is the electrometer value in electrical units from microDiamond detector readings and $K_{Diamond\ detector}^{ref}$ is the calibration coefficient factor, determined from cross-calibration.

Each measurement was repeated three times without separating the detector from the setup to obtain the measurement reproducibility.

a)   b)
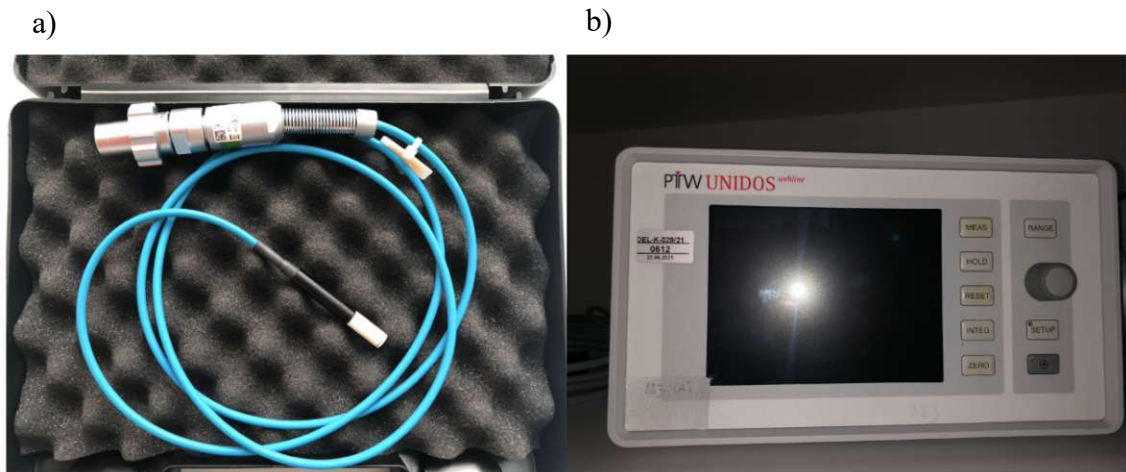
Figure 2-19: MicroDiamond detector (a) and UNIDOS electrometer (b)

Table 2-9 lists the position of the films and microDiamond detector in the phantom considering the water equivalent depth (WED in mm).

Three sets of films were placed directly between the phantom plates, except the last position, on which only one film was placed due to the steep dose gradient in the distal fall-off region. The stack of three films had 1 mm thickness. The final value was evaluated in the middle of film stack, therefore the measured point from films is 0.5 mm deeper in the SOBP.

The microDiamond detector was typically placed behind the three films. Moreover, the entrance material of detector is 1mm, therefore the measurement point of microDiamond detector was moved 2 mm deeper in SOBP.

Die approbierte gedruckte Originalversion dieser Diplomarbeit ist an der TU Wien Bibliothek verfügbar
The approved original version of this thesis is available in print at TU Wien Bibliothek.

TU Bibliothek, Your knowledge hub
WIEN

Table 2-9: Position of the films and the microDiamond detector (WED in mm).

	films [mm]	microDiamond detector [mm]
Position 1	5.5 mm	7 mm
Position 2	10.5 mm	12 mm
Position 3	15.5 mm	17 mm
Position 4	20 mm	21 mm

2.6 Data Evaluation

To investigate the depth-dose profiles in the small targets, as described in the previous subsections, films were fixed on the surface of the target layers. The microDiamond detector was positioned directly behind the target. The basic schematic of the complete setup is shown in Figure 2-5.

2.6.1 Quenching Correction Factor

Radiochromic films underestimate the dose in the Bragg peak area. This phenomenon is known as the "quenching effect" [37]. In this phenomenon the detector depends on a linear energy transfer (LET), where LET is increasing towards the end of SOBP [38]. This under response can be compensated by the proper quenching characterization. The factors were determined from the microDiamond detector measurements. The microDiamond detector was at the same position where the films were placed. The absolute dose was measured by microDiamond detector and the difference between the films and microDiamond detector was determined experimentally by the following equation:

$$Quenching\ correction\ factor = \frac{Dose_{diamond}}{Dose_{film}} \qquad (2-5)$$

Due to the steep slope of the dose-depth profile at the fourth position as well as the thickness of the three films and the 1 mm distance between the contact surface and the

active volume of the microDiamond detector, the quenching correction factor at the fourth position was determined from the calculation [39]. Table 2-10 lists the experimentally determined and calculated quenching factors for 4 depths:

Table 2-10: Experimentally determined and calculated values of the quenching factors

WED	Quenching factor
	Experimentally determined Values [Calculated values]
Position 1	1.04 [1.04]
Position 2	1.04 [1.06]
Position 3	1.06 [1.09]
Position 4	X [1.25]

2.6.2 Uncertainty Budget Estimation

To obtain the uncertainties of the microDiamond detector, each setup was irradiated 3 times at each position without separating the microDiamond detector from the setup. The uncertainties of the film's measurements were obtained as a combined uncertainty of the standard deviation of three films at each position and scanning each of the films three times with a flatbed scanner without changing the position of the films. The pixel values and the corresponding standard deviation of each of the scans were calculated in Gy with MATLAB. The independent uncertainties were combined using the root sum of squares (RSS) method.

2.6.3 Lateral Dose Profile

The beam profiles were obtained with RayStation's tool called "Lateral Dose Profile", which provides a line dose. Figure 2-20 shows the lateral dose profile of the phantom at the second position in TPS.

To plot the beam profiles of the films and compare them with RayStation results, the row in the films with the highest intensity was found. This row (see Figure 2-21) can

be determined by the deepest valley in horizontal integral projection (HIP) [40]. The mentioned row is where the lateral dose profile line has to be drawn. Figure 2-21 shows the HIP of a random film and the deepest valley in the y-axis which presents the row with the highest intensity.
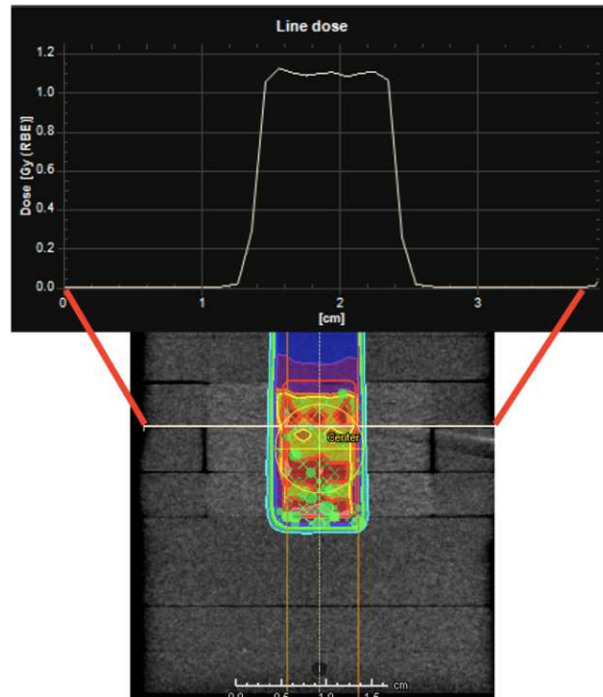
Figure 2-20: Lateral dose profile of phantom at position 2 in TPS
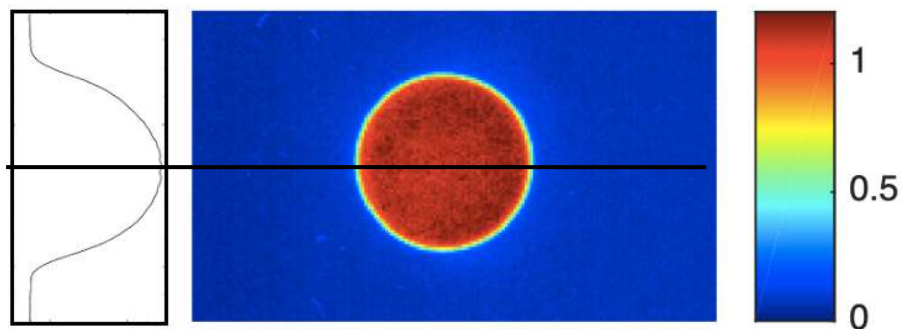
Figure 2-21: The deepest valley in HIP and the chosen row for the lateral dose profile

Chapter 3

Results

3.1 Overview of the Absorbed Dose Values

All experimentally determined doses were in the range between 0.86 Gy to 1.25 Gy and between 0.90 Gy to 1.22 Gy (without considering the fourth position) with the microDiamond detector and the EBT3 films, respectively. Table 3-1 and Figure 3-1 summarize the obtained results from all setups and measurement positions.

Regarding the range shifter setup: the results obtained from the combination of the range shifter with the iso-center airgap agreed well with the prescribed dose. Fairly large discrepancies were observed for the setup with airgap of 10 cm, with a maximum observed difference 25% between measured dose and prescribed dose.

Table 3-1: Dose values obtained by microDiamond detector and films for all the approaches.

Target Airgap Pre-absorber Aperture	microDiamond detector/ films at position 1 [Gy]	microDiamond detector/ films at position 2 [Gy]	microDiamond detector/ films at position 3 [Gy]	microDiamond detector/ films at position 4 [Gy]
T 1.2 cm, AG iso-center, Range shifter, A 1.5 cm	1.03/ 1.03	1.04/1.00	1.03/1.01	0.05/0.82
T 1.2 cm, AG iso-center, Bolus, A 1.5 cm	1.09/1.13	1.13/1.12	1.16/1.11	0.01/0.57
T 1.2 cm, AG 10 cm, Bolus, A 1.5 cm	0.98/1.00	0.99/1.02	0.96/1.04	0.07/1.03
T 1.2 cm, AG 10 cm, Range shifter, A 1.5 cm	1.22/1.19	1.11/1.20	1.25/1.22	0.21/1.24
T 1.2 cm, AG iso-center, Range shifter, no Aperture	1.05/1.01	1.06/1.02	1.07/1.01	0.05/0.87
T 0.8 cm, AG 10 cm, Range shifter, A 1.5 cm	1.17/1.16	0.86/1.17	1.00/1.17	0.11/1.08
T 0.8 cm, AG iso-center, Range shifter, A 1.1 cm	1.05/0.98	1.03/0.99	1.05/1.01	0.08/0.99

T 0.8 cm, AG iso-center, Range shifter, A 1 cm	1.02/0.98	1.04/1.00	1.06/1.03	0.86/1.16
T 0.8 cm, AG iso-center, Bolus, A 1.1 cm	0.93/0.92	0.93/0.91	0.87/0.90	0.00/0.19
T 0.8 cm, AG iso-center, Range shifter, A 1.1 cm 1 mm left	--**/0.95	--/0.99	--/0.99	--/0.44
T 0.8 cm, AG iso-center, Range shifter, A 1.1 cm 1 mm right	--/0.97	--/1.02	--/1.02	--/0.46
T 0.8 cm, AG iso-center, Range shifter, A 1.1 cm 2 mm left	--/0.95	--/0.99	--/1.00	--/0.46
T 0.8 cm, AG iso-center, Range shifter, A 1.1 cm 2 mm right	--/0.96	--/0.98	--/1.00	--/0.47
T 0.8 cm, AG iso-center, Range shifter, A 1.1cm Aperture not including in TPS	1.14/1.10	1.12/1.12	1.11/1.09	0.37/0.08

** The measured doses with microDiamond detector are not available in these cases.
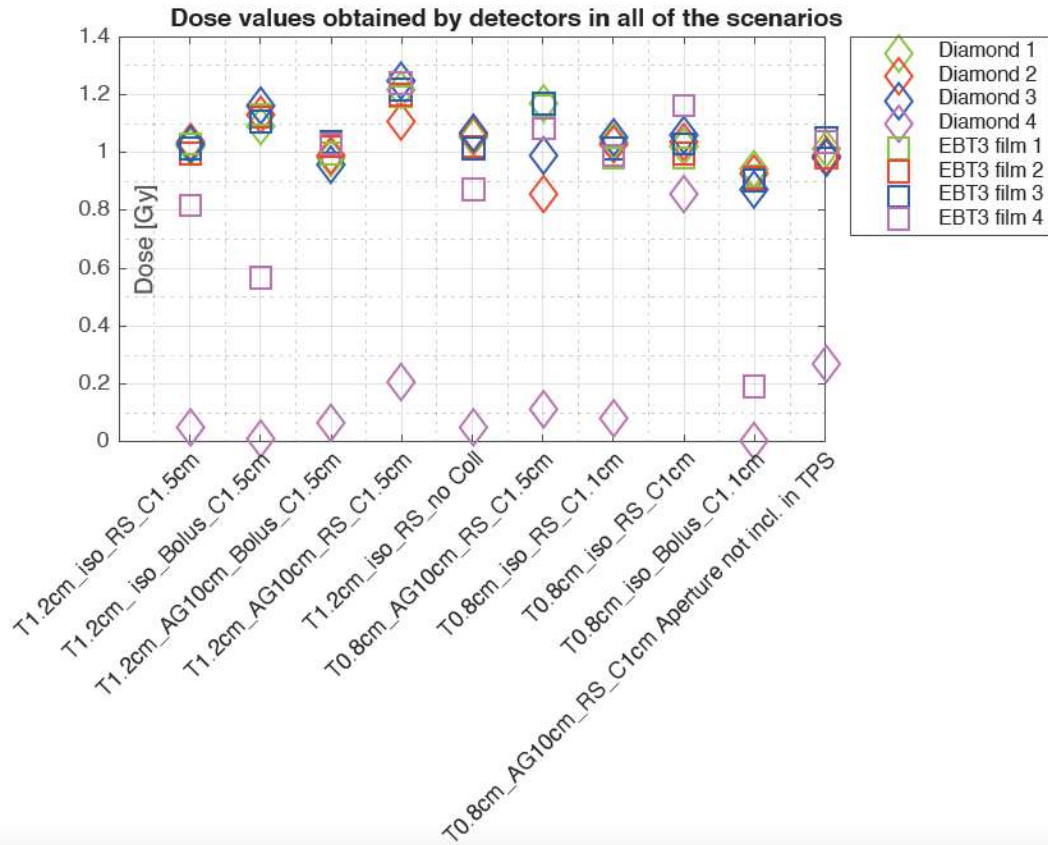
Figure 3-1: A comparison of the obtained dose values with a microDiamond detector and films at four positions for all measured setups

3.2 Setup Scenarios

Various setups were designed to test the impact of an aperture or a pre-absorber on the target dose distribution. The results of the setups are described in the following subsections.

3.2.1 Comparison of the Dose Distribution with and without an Aperture

Figure 3-2 presents the color-map of results when using an aperture in the setup, with an opening of 1.1 cm as well as the results without any aperture. The red color corresponds to a high dose (maximum 1.2 Gy) and blue corresponds to a low dose value (minimum 0 Gy). The target border is determined by dark circles. In case no aperture was used, the dose was spread over the entire target region as well as the phantom area.

Table 3-2 lists the measured dose values obtained from the films and microDiamond detector. The uncertainty in the microDiamond detector was smaller than the number of digits displayed behind the comma and was therefore not reported. The corresponding uncertainties for the EBT3 films are presented in Table 3-2.

Table 3-2: List of measured dose values with films and microDiamond detector.

	With Aperture		Without Aperture	
	Films [Gy]	mD [Gy]	Films [Gy]	mD [Gy]
Position 1	0.99±0.07	1.05	1.05±0.08	1.01
Position 2	0.99±0.07	1.03	1.04±0.10	1.05
Position 3	1.01±0.07	1.05	1.04±0.11	1.01
Position 4	1.00±0.00	0.08	1.11±0.05	0.55
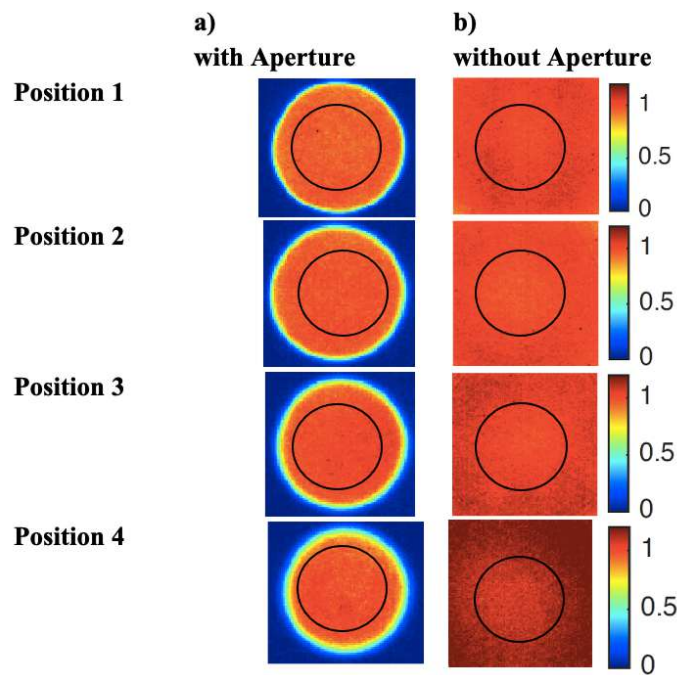
Figure 3-2: The color-map of the dose distribution in phantom when an aperture was used (a) and when no aperture was used (b). The dark circles illustrate the border of the target

Figure 3-3 displays the influence of the aperture on the dose distribution inside the target. The lateral dose profiles of the phantom are shown at position 2 with and without an aperture. The yellow semi-transparent shadow indicates the target area. The aperture

limits the irradiation field to the target significantly, whereas the dose of 1 Gy or more was measured outside the target when no aperture was used.
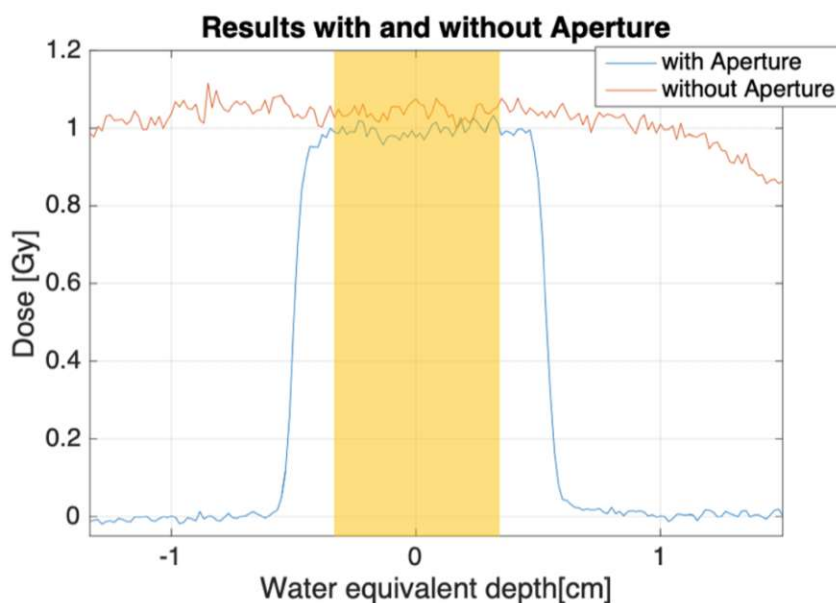
Figure 3-3: A comparison of dose distribution in EBT3 films for the target size of 0.8 cm and collimator of 1.1 cm at position 2 with and without an aperture

3.2.2 Limitation of Aperture Size

The measured dose values inside the target of 0.8 cm with the 1.1 cm and 1 cm aperture and the related uncertainties are summarized in Table 3-3. In both cases, the prescribed dose could be achieved. The uncertainties of the films with the 1.1 cm aperture were slightly smaller than for the 1 cm aperture.

Figure 3-4 shows the depth dose distribution obtained by the microDiamond detector, films with the corresponding uncertainties and the predicted dose by treatment planning system for aperture with the opening size of 1.1 cm and 1 cm, respectively.

As seen in Figure 3-4 and Table 3-3, the behavior of both cases was very similar, and the larger differences were observed only at the fourth measured position within the phantom. Moreover, the obtained uncertainties were also rather small.

Table 3-3: List of the measured dose values with films and microDiamond detector for the comparison of two different aperture sizes.

	1.1 cm Aperture		1 cm Aperture	
	Films [Gy]	mD [Gy]	Films [Gy]	mD [Gy]
Position 1	0.99±0.07	1.05	1.00±0.10	1.02
Position 2	0.99±0.07	1.03	1.01±0.10	1.04
Position 3	1.01±0.07	1.05	1.03±0.10	1.06
Position 4	0.99±0.00	0.08	1.13±0.02	0.86

Even though the TPS predictions for 1 cm aperture were worse compared to 1.1 cm aperture, only a slight difference was observed with the measurements (films and microDiamond detector).
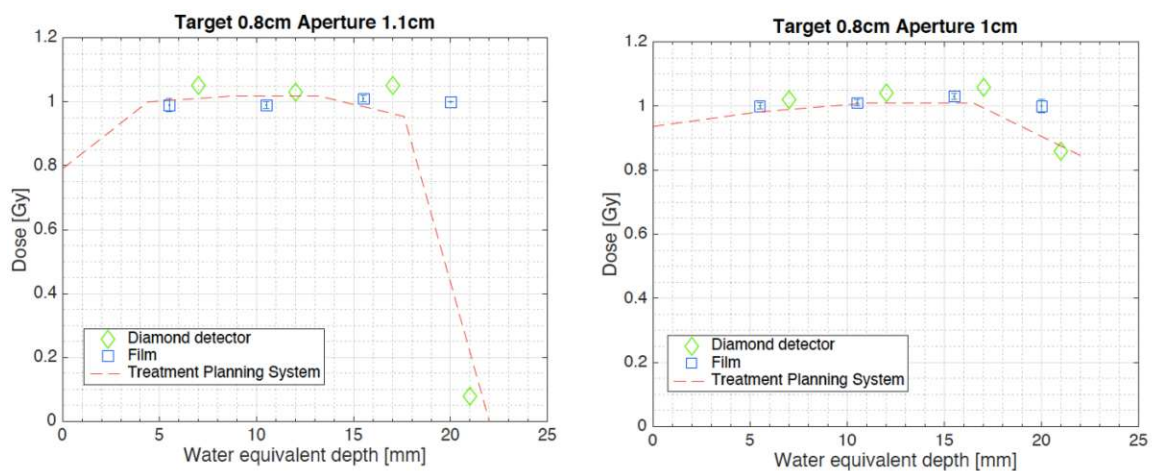

Figure 3-4: Depth dose distribution obtained with microDiamond detector, films and TPS for a target with the diameter of 0.8 cm and an aperture with the opening size of 1.1 cm (a) and 1 cm (b)

The lateral two-dimensional dose distributions in films when the 1.1cm and 1 cm apertures were used, is depicted in Figure 3-5. The dose across the target was homogeneous in both cases.
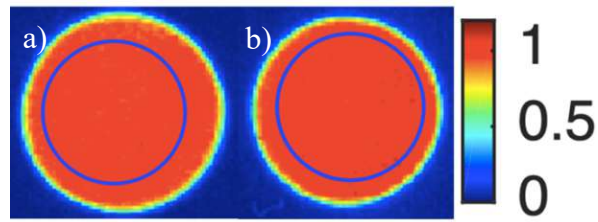
Figure 3-5: The dose distribution color-map with 1.1 cm aperture (a) and 1 cm aperture (b). The corresponding color bar can be seen on the right side of the image.

3.2.3 Comparison of Different Pre-absorbers and Different Target Sizes

Different Pre-absorbers

Tables 3-4 and 3-5 provide the results of the predicted dose values from the TPS and the absolute doses measured with the microDiamond detector and the films when either a bolus or the range shifter was used in the setup.

The setup with the range shifter showed a good agreement between the prescribed, measured and calculated dose. The setup with the bolus led to higher measured and calculated dose values compared to the prescribed dose.

Table 3-4: Obtained dose values in the setup with bolus.

	TPS [Gy]	mD [Gy]	EBT-3 films [Gy]
position 1	1.13	1.09	1.13$\pm$0.28
position 2	1.11	1.13	1.12$\pm$0.35
position 3	1.13	1.16	1.11$\pm$0.34
position 4	0.08	0.01	0.57$\pm$0.02

Table 3-5: Obtained dose values in the setup with range shifter.

	TPS [Gy]	mD [Gy]	EBT-3 films [Gy]
position 1	0.98	1.03	1.03±0.09
position 2	0.99	1.04	1.00±0.10
position 3	0.98	1.03	1.01±0.09
position 4	0.26	0.05	0.82±0.11

Figures 3-6 and 3-7 show the lateral dose profiles obtained from the films and TPS at position 2 with the bolus and the range shifter as pre-absorber, respectively. As it is shown in Figure 3-6, the dose was not homogeneously distributed inside the target when the bolus was used as the pre-absorber. The maximum measured dose at the center of the target was 16% higher than the prescribed dose. The dose distribution was dome-shaped and decreased gradually farther away from the center of the target. The lateral penumbra (LP$_{80-20}$) for bolus was 3 mm.
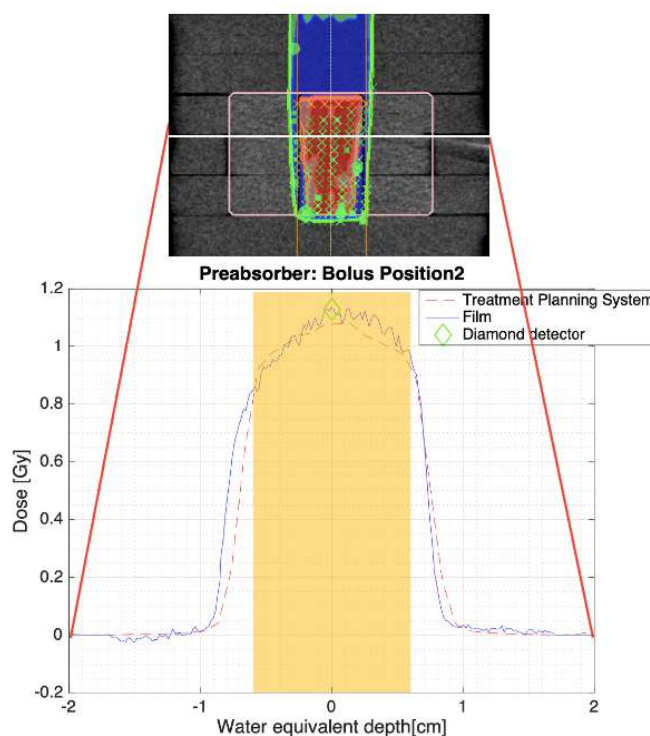
Figure 3-6: Lateral dose profile of the phantom at position 2 with bolus as the pre-absorber. The yellow semi-transparent shadow show the area of the target. The green diamond marker indicates the absolute dose at the center of the target measured by the microDiamond detector.

Figure 3-7 shows the homogeneousness of the dose distribution inside the target when the range shifter was used as the pre-absorber. The depth-dose profile inside the target was flat and the dose was distributed uniformly across the target. The lateral penumbra (LP_{80-20}) for range shifter was 0.5 mm.
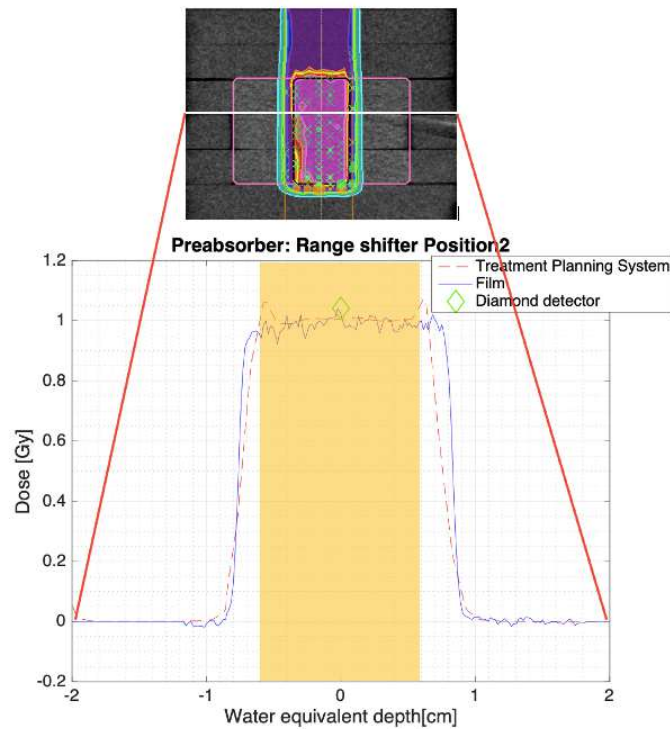

Figure 3-7: Lateral dose profile of the phantom at position 2 with range shifter as the pre-absorber

Figure 3-8 shows the colormap of the dose distribution in films at position 2 when the bolus and the range shifter were used as pre-absorber.
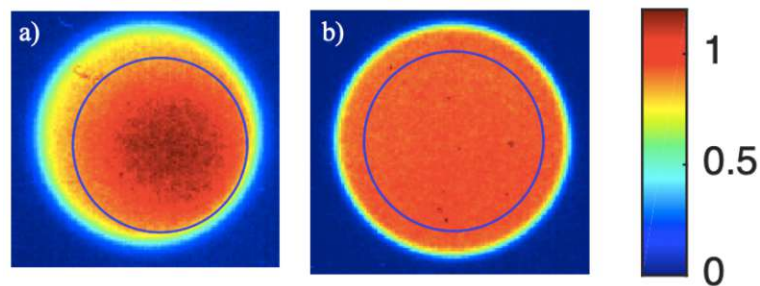

Figure 3-8: The dose distribution colormap in films when bolus (a) and range shifter (b) were used.

It is worth to mention that after this investigation, the TPS plans for the bolus setup optimized and the dose distribution was improved in TPS. However, the outcome with the range shifter could not be reached.

Different Target Sizes

Table 3-6 lists the dose values measured with the microDiamond detector and films in four positions of the phantom for 0.8 cm and 1.2 cm targets. This comparison led to similar results and comparable dose distributions inside the target.

Table 3-6: Dose values of 0.8 cm and 1.2 cm targets.

	Dose of 0.8 cm Target [Gy]		dose of 1.2 cm Target [Gy]	
	Films	**mD detector**	**Films**	**mD detector**
position 1	0.99±0.07	1.05	1.02±0.09	1.03
position 2	0.99±0.07	1.03	0.99±0.10	1.04
position 3	1.01±0.07	1.05	0.99±0.09	1.03
position 4	1.00±0.00	0.08	0.81±0.11	0.05

Figure 3-9 depicts the comparison between lateral dose profiles for target sizes of 1.2 cm and 0.8 cm at the first three positions. The blue graph shows the lateral dose profile of the larger target and the red graph shows the lateral dose profile of the smaller target. The blue and red arrows determine the target area. The absolute dose measured by the microDiamond detector is shown as a diamond shaped marker. The measurements of the microDiamond detector showed a better agreement with the EBT3 film in the larger target, as can be seen in Table 3-6 and also in Figure 3-9. The dose was distributed uniformly across both targets.

a)

Dose line of large and small target at position 1

b)

Dose line of large and small target at position 2
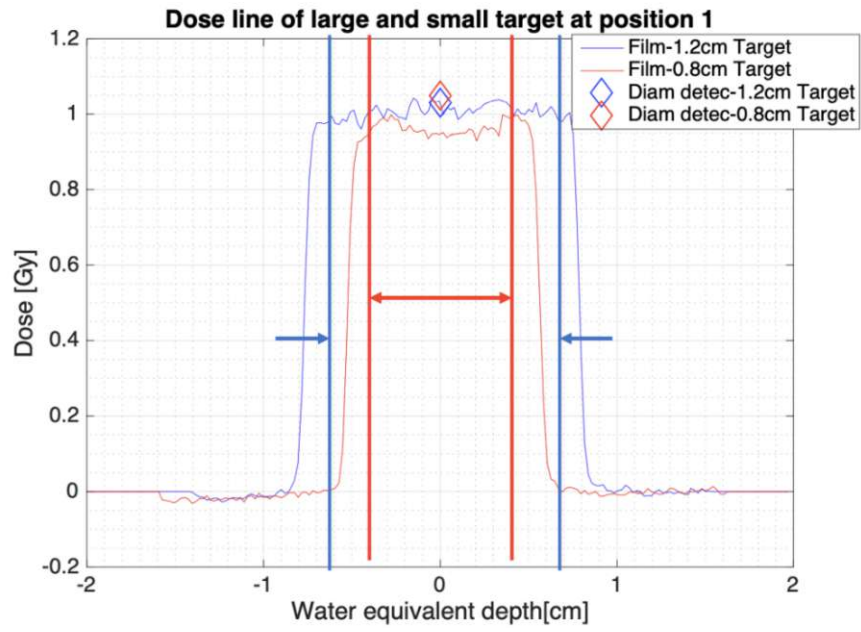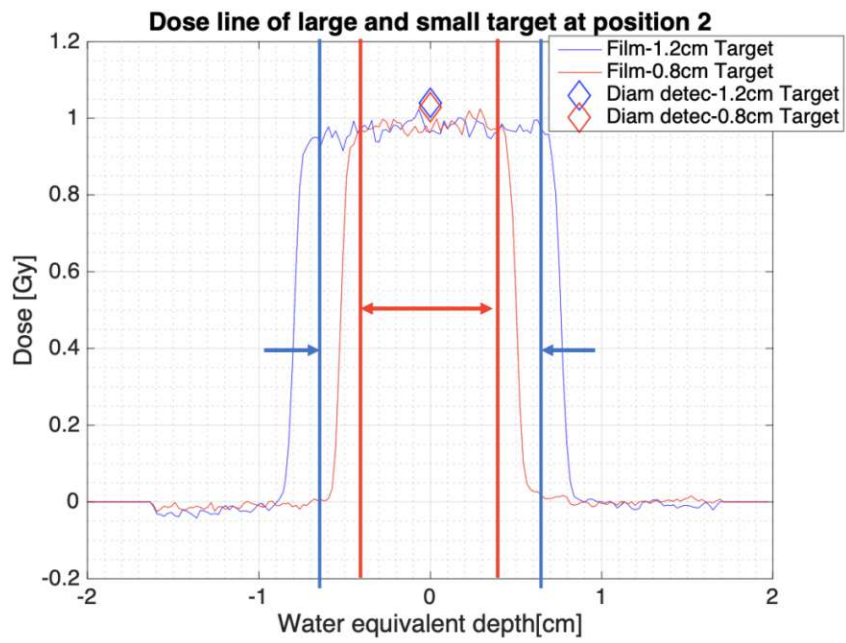
c)
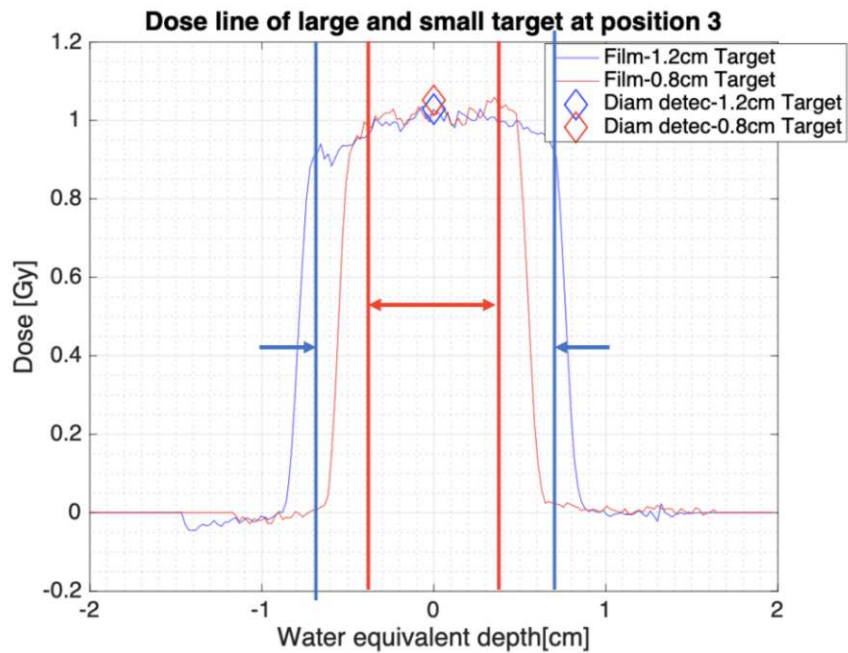
Figure 3-9: Dose profiles of films and microDiamond detector at position 1 (a), position 2 (b) and position 3 (c) within the phantom. Blue and red arrows show the target sizes of 1.2 cm and 0.8 cm respectively.

3.2.4 Positioning Accuracy of the Aperture

Lateral Shifts

Figure 3-10 depicts the SOBPs of the irradiated films with the corresponding uncertainties at four positions while the aperture was centered to the position of the target. Additionally, the results from lateral misplacements of 1 mm and 2 mm are shown. As seen in this figure as well as in Table 3-7, the largest difference was observed at the fourth measurement position.
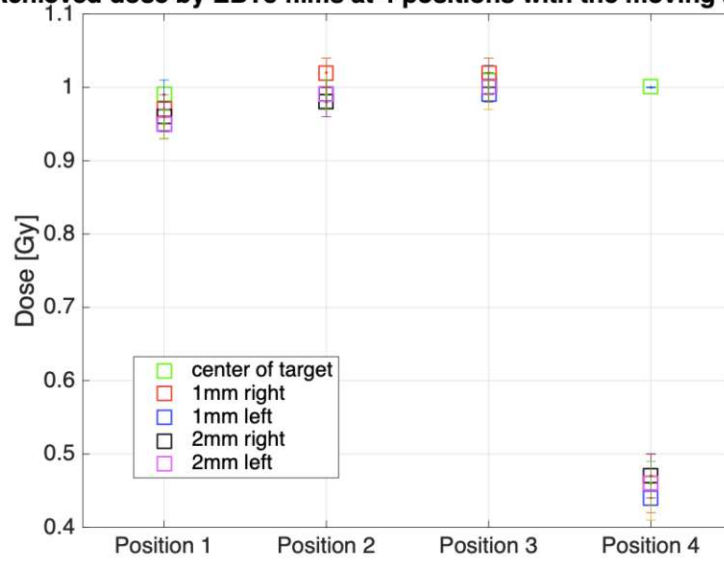
Figure 3-10: Depth dose values determined from the films when the aperture was centered to the respect of the target (green), shifted by 1mm to the right side (red), 1mm left (blue), 2mm right (black) and 2mm left (magenta)

Table 3-7: A summary of dose values measured with films and the corresponding uncertainties, which are plotted in Figure 3-10.

	Center of Target [Gy]	1mm right [Gy]	1mm left [Gy]	2mm right [Gy]	2mm left [Gy]
Position 1	0.99±0.07	0.97±0.04	0.95±0.04	0.96±0.04	0.95±0.04
Position 2	0.99±0.07	1.02±0.04	0.99±0.04	0.98±0.04	0.99±0.04
Position 3	1.01±0.07	1.02±0.04	0.99±0.04	1.00±0.04	1.00±0.04
Position 4	1.00±0.00	0.46±0.06	0.44±0.05	0.47±0.05	0.46±0.05

Figure 3-11 shows the dose distributions when the aperture was placed at the center of the target as well as laterally shifted to the left and right. The dose across the target was homogeneously distributed in all five cases.
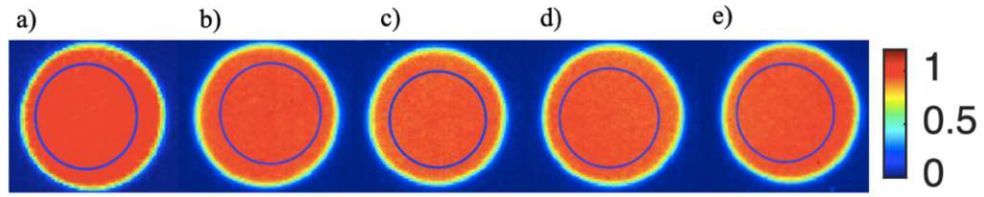
Figure 3-11: Dose distribution color-map. Aperture at the center of the target (a), 1mm right (b), 1mm left (c), 2mm right (d) and 2mm left (e)

Although Figures 3-10 and 3-11 show that the dose was homogeneously distributed inside the target and along the SOBP, Figures 3-12 and 3-13 show that moving the aperture to the right and left influenced the flattened area of the lateral dose profiles.

Figure 3-13 is a zoomed version of Figure 3-12 in order to highlight the differences of five measurements inside the target.
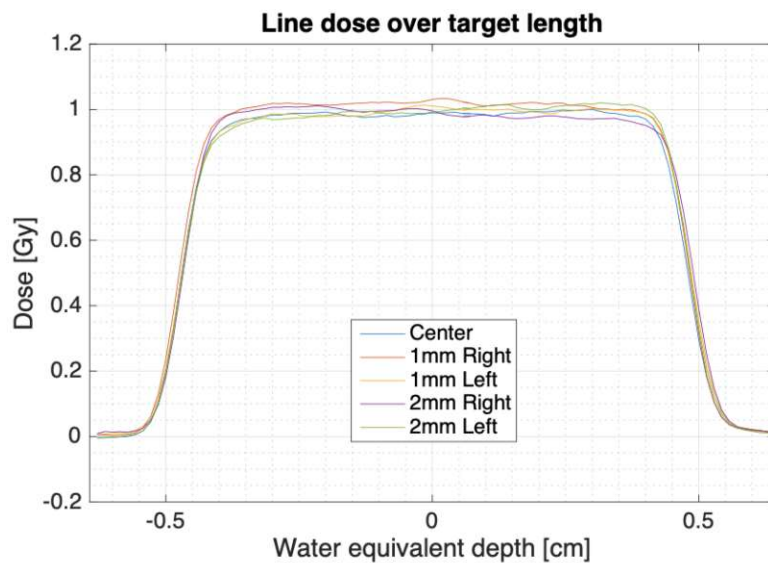
Figure 3-12: Lateral dose profiles when an aperture was laterally shifted. Aperture at the center (blue), 1mm right (red), 2mm right (yellow), 1mm left (magenta) and 2mm left (green)
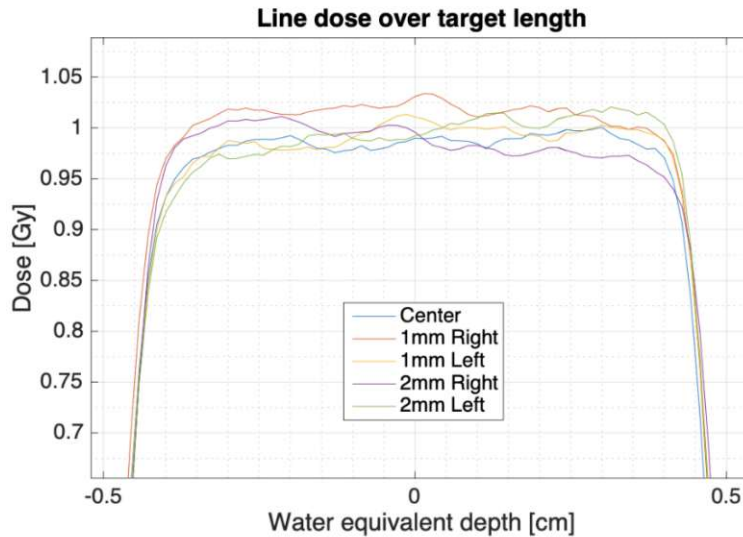
Figure 3-13: A more detailed view of Figure 3-12.

As seen in Figures 3-12 and 3-13, the behavior of the profiles with a 2 mm shift to the right and left was not similar to the profile with the aperture at the center. When the aperture was in the center of the target, the flattened region was much flatter. But by moving the aperture 2 mm to the right side, more dose was accumulated on the left side and by moving the aperture 2 mm to the left side, more dose was accumulated to the right side.

3.2.5 Aperture not modeled in TPS

Table 3-8 lists dose values measured with microDiamond detector and films in four positions of the phantom when the aperture was considered in TPS and also used during irradiation and when the aperture was not considered in TPS and placed in front of the setup.

When no aperture was considered in TPS (Figure 3-14), an overdose of 7% was detected by microDiamond detector and 10% more dose was measured by films (without considering the fourth position). The uncertainties were also higher for this setup compared to other investigated setups.

Table 3-8: Determined absorbed dose in the target, while including and not including the aperture in TPS.

	Aperture including in TPS		Aperture not including in TPS	
	mD [Gy]	Film [Gy]	mD [Gy]	Film [Gy]
Position 1	1.05	0.99±0.07	1.14	1.10±0.10
Position 2	1.03	0.99±0.07	1.12	1.12±0.10
Position 3	1.05	1.01±0.07	1.11	1.09±0.12
Position 4	0.08	1.00±0.00	0.37	0.08±0.02
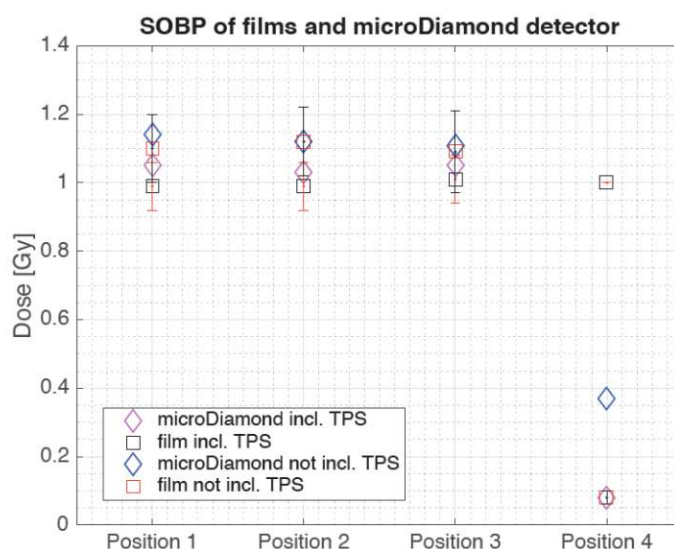
Figure 3-14: Depth dose values obtained in the setup where the aperture was not modeled in TPS.

Figure 3-15 shows the color-map of the dose distribution in the phantom acquired from the films. Figure 3-15 (a) illustrates the dose distribution inside the phantom when the 1.1 cm aperture was placed in front of the phantom during irradiation as well as included in TPS.

Figure 3-15 (b) shows the dose distribution inside the phantom when the aperture was simply placed in front of the phantom during radiation without considering it in TPS. The dose decreased gradually at the edges, which leads to larger penumbra.
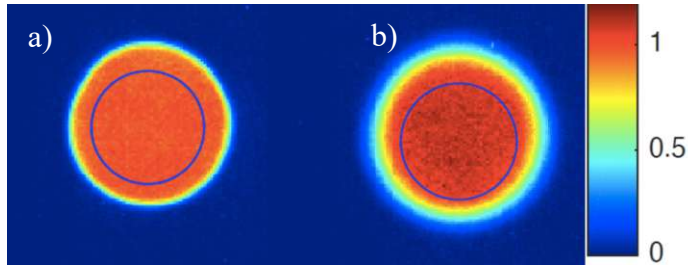
Figure 3-15: The comparison of the dose distribution in the phantom with aperture modeling in TPS (a) and without modeling it in TPS (b)
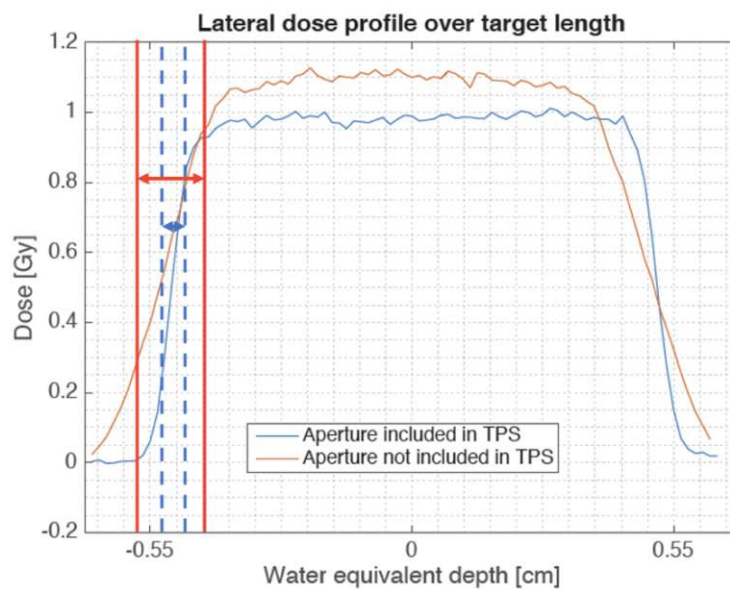
Figure 3-16: Lateral dose profile and lateral penumbra (LP_{80-20}) of the described approaches. The blue line represents the aperture included in TPS, the red line indicates no aperture.

Figure 3-16 illustrates the lateral dose profile of two approaches. The penumbra (LP_{80-20}) 0.5 mm for the aperture included in TPS, while it was 1.5 mm when the aperture was not included in TPS.

Chapter 4

Discussion

Commercial small animal irradiators are only accessible for photons and small irradiation studies with particle irradiation is currently performed in clinical facilities [41, 42]. Furthermore, the existing TPS is not designed for small field irradiation [43].

In the frame of this thesis, small fields relevant to the small animals were irradiated with proton beams at the MedAustron facility. Limitations of the equipment and tools designed for patients were investigated. According to [44], small field dosimetry is relevant for the fields smaller than 4.5 cm in diameter. In the scope of this work, the absolute dose at the center of the target was measured with the microDiamond detector and the dose distribution was assessed using the EBT3 films. As shown in [45], the use of a collimator may sharpen the lateral dose gradient. Since the structures in small animals are very small, the size of the beam is relatively large compared to the target, therefore an aperture has to be placed in the beam pathway to restrict the irradiation to the target. The relevant targets for small animals are defined at very shallow depths and hence, a pre-absorber should be placed in front of the target to reduce the penetration depth. The beam shaping devices and pre-absorbers were tested in different setups.

One of the main objectives of this thesis was to investigate the influence of an aperture on the dose distribution inside the small targets and the dose calculation performance

of TPS with and without an aperture. As mentioned in "Results" in subsection 3.2.1, dose was properly predicted by the dose calculations in the TPS for the setup with range shifter and a good agreement between the predictions and verification measurements was found for both scenarios (with and without aperture). As shown in Figures 3-2 and 3-3 the dose around the target was improved significantly with an aperture, whereas in the absence of the aperture, the whole target as well as the surrounding area was irradiated with a relatively high dose. Therefore, the rest of the measurements were performed with the presence of an aperture in front of the setup.

The limitation of the smallest possible aperture for a certain target size was tested with two different aperture openings. For the 0.8 cm target, two collimators with the opening size of 1 cm and 1.1 cm were generated. As published by Wang et. al. [46] smaller apertures provide the optimum tissue sparing around the target but are unable to reach the same dose homogeneity inside the target as larger apertures. Furthermore, Kacperek [47] reported that the penumbra shape remains constant while the entrance dose increases with decreasing collimator diameter. From the results given in this thesis, two investigated aperture sizes were very comparable. The comparison of the dose distribution in films, Figure 3-5, verifies the homogeneities in both of the setups. As listed in Table 3-3 and shown in Figure 3-4 measurement results from films in both of the setups agreed well with each other as well as with the predicted dose in TPS. Although the uncertainties in the smaller aperture (1 cm) are a bit higher.

To reduce the beam range and to irradiate the shallow targets, either a range shifter which is located in the nozzle or a bolus that is placed on the phantom's surface has to be employed. Depending on the material and the thickness of the target, the pre-absorbers broaden the beam [48]. The goal of the measurements performed in this thesis was to compare the effect of the bolus and the range shifter on the dose distribution inside the target. As shown in Figures 3-6 and 3-7, the results, obtained with the microDiamond detector and the EBT3 films in the setup with the range shifter, showed that the lateral dose profile was flatter and more homogeneous than the measurements with the bolus as a pre-absorber. As listed in Tables 3-4 and 3-5, the measurement results with the range shifter agreed almost perfectly with the prescribed dose, while the values with bolus were up to 10% higher than the prescribed dose. The range shifter broadens the beam, this broadening and aperture are properly taken into account in dose

calculations of the TPS and this setup resulted in a good agreement with the prescribed dose. The usage of the bolus as pre-absorber caused a dome-shaped lateral dose distribution present due to the scatter on the aperture and inside the bolus (see Figure 3-6) and this scatter is not properly predicted by dose calculations. As shown in Figure 3-8, the dose is not homogeneously distributed inside the target, and there is more dose concentrated at the center of the target than the edges when the bolus was employed. The dose inhomogeneities in the target might increase the risk of hot and cold spots inside of the target volume. Whereas, the results acquired from the range shifter showed a homogenous dose distribution inside the target. After the irradiation, the treatment plan for bolus was recreated and re-optimized. The results were better than the current results. Nevertheless, the improved plans never reached the outcome of the setup with range shifter.

Two small targets (0.8 cm and 1.2 cm) were delineated, the treatment plans were created and the prescriptions were delivered to the phantom. In order to determine the dose inside the target, the films and the microDiamond detector were fixed on the target's surface. As listed in Table 3-6, the absolute dose measured with the microDiamond detector was nearly identical for both target sizes. The comparison of the averaged dose distributed inside the target measured with the EBT3 films in both cases showed a good agreement considering only the first three positions. In positions 2 and 3, the measurements of the films in both target sizes showed good conformity. The dose inside the smaller target (0.8 cm) is distributed as homogeneous as the dose inside the larger target (1.2 cm) (see Figure 3-9, the flattened area inside the targets). As seen in figure 3-7 (a), the dose inside the smaller target (diameter: 0.8 cm) at the first position was lower than the larger target (diameter: 1.2 cm). Here the limitation of TPS and the performance of dose calculations for small fields could be reached.

Since the results from the range shifter were better than the ones obtained with the bolus and the results acquired from the smaller target were comparable with the larger target, the experiments were continued with these settings. The dose values measured with EBT3 films had the agreement with the prescribed dose when the aperture was well aligned with the center of the target (Table 3-7). The comparison of the results of the EBT3 films from the SOBP measurement in Figure 3-10 showed that the results vary by changing the position of the aperture relative to the target. Based on the results in

Table 3-7 and Figure 3-10, the lateral shifts of the aperture have an influence on the dose distribution inside the target. The largest disagreement was obtained for 2 mm collimator shift. When the aperture was shifted to the right, less dose was delivered to the right part of target and vice versa. As a result, the position accuracy of the setup plays an important role in small field irradiation and the misplacements larger than 1 mm lead to dose differences between the prescribed and measured dose larger than 5%.

In-vivo studies do not always include an aperture to reduce the dose to surrounding tissues. Moreover, since the dedicated TPSs for small animals are rather limited, apertures are not included in the treatment planning process. These constrains might lead to acute side effects and animal discomfort. The importance of considering the aperture in TPS was investigated in this work. As it can be seen in Table 3-8, there is a difference between the 2 setups. When the aperture is not included in TPS the dose exceeds the prescribed dose by 12%. In addition, the uncertainties are also larger. Figure 3-14 shows the delivered SOBP to the phantom. When the aperture is not included in TPS, the results have larger disagreement to the prescribed dose. Figure 3-15 determines the border of the targets in both of the setups. It is evident that when the aperture is placed simply in front of the setup, there is more penumbra around the target and more dose is applied inside the target. As shown in Figure 3-16, the lateral penumbra (LP_{80-20}) caused by not including the aperture in TPS is three times larger the one with aperture in TPS.

Chapter 5

Conclusion and Outlook

The aim of this study was to explore the limitations of small field irradiation at MedAustron with equipment developed for patients. The dose was calculated by the TPS and dosimetric verification was performed experimentally.

From the observed findings (cf. subsection 3.2.1) it can be concluded that the presence of the aperture is essential for small field irradiation to minimize the dose to healthy tissue and improve the lateral penumbra. Different aperture sizes and target sizes relevant for small animal irradiation were investigated.

The results in this study led to the conclusion that the setup with range shifter provided better target dose distribution and smaller lateral penumbra compared to the setup with the bolus. Therefore, for small field irradiation at MedAustron, the usage of the range shifter as a pre-absorber in combination with a larger airgap (> 50 cm) is recommended.

The results of the different target diameters indicate that even the smallest investigated target size with a diameter of 0.8 cm had a good target coverage. The positioning accuracy of the setup as well as the aperture is important for small field irradiation. It was shown that misplacement of the aperture relative to the phantom setup is larger than 1 mm may lead to dose differences of up to 8% inside the target. The aperture

should be included in the treatment planning process. It was demonstrated that when the aperture was placed into the beamline without considering it in TPS, the dose difference between the prescribed and measured dose was 12%.

Regarding the outlook for the preparatory work in small animal irradiation at MedAustron, further investigations are planned for even smaller apertures and field sizes. Additionally, a heterogeneous phantom with various materials representing animal tissues needs to be included for future studies to further benchmark the TPS.

Bibliography

[1] K. Souris, "Accurate assessment of proton therapy treatments : fast Monte Carlo dose engine and extensive robustness tests," 2018, [Online]. Available: https://dial.uclouvain.be/pr/boreal/object/boreal:192917.

[2] S. Giordanengo, L. Manganaro, and A. Vignati, "Review of technologies and procedures of clinical dosimetry for scanned ion beam radiotherapy," *Phys. Medica*, vol. 43, no. October, pp. 79–99, 2017, doi: 10.1016/j.ejmp.2017.10.013.

[3] D. Andisco, S. Blanco, and A. E. Buzzi, "Dosimetery in Radiology," *Rev. Argentina Radiol.*, vol. 78, no. 2, pp. 114–117, 2014, doi: 10.1016/j.rard.2014.06.010.

[4] R. Wideröe, "Über ein neues Prinzip zur Herstellung hoher Spannungen," *Arch. für Elektrotechnik*, vol. 21, no. 4, pp. 387–406, 1928, doi: 10.1007/BF01656341.

[5] H. Fuchs, "Development and Validation of Helium Ion Beam Dose Calculation Doctoral thesis at the Medical University of Vienna for obtaining the academic degree," Medical University of Vienna, 2014.

[6] R. Mohan and D. Grosshans, "Proton therapy – Present and future," *Adv. Drug Deliv. Rev.*, vol. 109, pp. 26–44, 2017, doi: 10.1016/j.addr.2016.11.006.

[7] B. T. E.-C. Onal, "Advanced Radiation Treatment Planning of Prostate Cancer," Rijeka: IntechOpen, 2018, p. Ch. 3.

[8] A. Thummerer, "Characterization and preparation of thermoluminescence dosimeters for surface and in vivo dose measurements," 2018, [Online]. Available: https://resolver.obvsg.at/urn:nbn:at:at-ubtuw:1-111953.

[9] S. Gagnebin, "Experimental determination of the absorbed dose to water in a scanned proton beam using a water calorimeter and an ionization chamber," niversity of Neuchâtel, 2010.

[10] E. B. Podgoršak, *Radiation Physics for Medical Physicists*. Springer International Publishing, 2016.

[11] D. Schardt, T. Elsässer, and D. Schulz-Ertner, "Heavy-ion tumor therapy: Physical and radiobiological benefits," *Rev. Mod. Phys.*, vol. 82, no. 1, pp. 383–425, 2010, doi: 10.1103/RevModPhys.82.383.

[12] INTERNATIONAL ATOMIC ENERGY AGENCY, *Diagnostic Radiology Physics: a handbook for teachers and students*. IAEA, Vienna, 2014.

[13] S. Haupt, "Dose area product measurements with a novel large area ionization chamber in scanned proton beams," Fakultät für Physik der Technischen Universität Wien, 2019.

[14] A. Balz, "Surface Proton Dosimetry and its clinical application," 2018.

[15] A. Hofer, "Dose distribution measurements with Octavius 729XDR and their applications at MedAustron," Technische Universität Wien, 2018.

[16] E. B. Podgorsak, *Radiation Oncology Physics: A Handbook for Teachers and Students*. Vienna: International Atomic Energy Agency, 2005.

[17] B. Rossi and H. H. Staub, "Ionization Chambers and Counters: Experimental Techniques," McGraw-Hill Book Company, 1949.

[18] C. L. Luke and W. Yuan Chien-Shiung, "Methods in Experimental Physics," *Nucl. Physics. Acad. Press*, vol. 5 Part A, 1961.

[19] O. J. Brace *et al.*, "Evaluation of the PTW microDiamond in edge-on orientation for dosimetry in small fields," *J. Appl. Clin. Med. Phys.*, vol. 21, no. 8, pp. 278–288, 2020, doi: 10.1002/acm2.12906.

[20] "User Manual microDiamond Type 60019," PTW-Freiburg, Germany, 2016.

[21] W. Parwaie, S. Refahi, B. Farhood, and H. Services, "Different Dosimeters / Detectors Used in Small-Field Dosimetry : Pros and Cons Different Dosimeters / Detectors Used in Small - Field Dosimetry : Pros and Cons," no. July, 2018, doi: 10.4103/jmss.JMSS.

[22] N. C. Knutson, "Evaluation of a Proton Pencil Beam Algorithm for," 2012.

[23] D. C. Westerly, X. Mo, W. A. Tomé, T. R. Mackie, and P. M. J. DeLuca, "A generalized 2D pencil beam scaling algorithm for proton dose calculation in heterogeneous slab geometries.," *Med. Phys.*, vol. 40, no. 6, p. 61706, Jun. 2013, doi: 10.1118/1.4804055.

[24] R. Fujimoto, T. Kurihara, and Y. Nagamine, "GPU-based fast pencil beam algorithm for proton therapy.," *Phys. Med. Biol.*, vol. 56, no. 5, pp. 1319–1328, Mar. 2011, doi: 10.1088/0031-9155/56/5/006.

[25] Joris Hartman, "Dosimetric feasibility of real-time MRI-guided proton therapy," Utrecht University, The Netherlands, 2018.

[26] K. Faiz M. and G. John P., *Khan's the Physics of Radiation Therapy*. Lippincott Williams & Wilki, 2014.

[27] M. Benedikt, J. Gutleber, M. Palm, W. Pirkl, U. Dorda, and A. Fabich, "Overview of the MedAustron design and technology choices," *IPAC 2010 - 1st Int. Part. Accel. Conf.*, vol. 1, no. V, pp. 109–111, 2010.

[28] E. R. Biglin, G. J. Price, A. L. Chadwick, A. H. Aitkenhead, K. J. Williams, and K. J. Kirkby, "Preclinical dosimetry: Exploring the use of small animal phantoms," *Radiat. Oncol.*, vol. 14, no. 1, pp. 1–11, 2019, doi: 10.1186/s13014-019-1343-8.

[29] K. T. Butterworth, "Evolution of the Supermodel: Progress in Modelling Radiotherapy Response in Mice," *Clin. Oncol.*, vol. 31, no. 5, pp. 272–282, 2019, doi: 10.1016/j.clon.2019.02.008.

[30] B. Bednarz, J. Daartz, and H. Paganetti, "Dosimetric accuracy of planning and delivering small proton therapy fields," *Phys Med Bio*, vol. 23, no. 1, pp. 1–7, 2010, doi: 10.1088/0031-9155/55/24/003.Dosimetric.

[31] L. Grevillot, M. Stock, and S. Vatnitsky, "Evaluation of beam delivery and ripple filter design for non-isocentric proton and carbon ion therapy," *Phys. Med. Biol.*, vol. 60, pp. 7985–8005, Sep. 2015, doi: 10.1088/0031-9155/60/20/7985.

[32] S. H. Lee *et al.*, "Evaluation of radioactivity induced by patient-specific devices in proton therapy," *J. Korean Phys. Soc.*, vol. 60, no. 1, pp. 125–128, 2012, doi: 10.3938/jkps.60.125.

[33] L. T. and M. C-M., "Proton and Carbon Ion Therapy," pp. 1–2, 1979, doi: 10.1093/oxfordjournals.alcalc.a044152.

[34] A. Niroomand-Rad *et al.*, "Radiochromic film dosimetry: Recommendations of AAPM Radiation Therapy Committee Task Group 55," *Med. Phys.*, vol. 25, no. 11, pp. 2093–2115, 1998, doi: 10.1118/1.598407.

[35] S. Devic, N. Tomic, and D. Lewis, "Reference radiochromic film dosimetry: Review of technical aspects," *Phys. Medica*, vol. 32, no. 4, pp. 541–556, 2016, doi:

10.1016/j.ejmp.2016.02.008.

[36]   A. CARLINO, "Implementation of advanced methodologies in the commissioning of a Light Ion Beam Therapy facility," University of Palermo, Italy., 2017.

[37]   S. J. Doran, T. Gorjiara, J. Adamovics, Z. Kuncic, A. Kacperek, and C. Baldock, "The quenching effect in PRESAGE® dosimetry of proton beams: Is an empirical correction feasible?," *J. Phys. Conf. Ser.*, vol. 573, no. 1, pp. 2–7, 2015, doi: 10.1088/1742-6596/573/1/012043.

[38]   R. Castriconi *et al.*, "Dose-response of EBT3 radiochromic films to proton and carbon ion clinical beams," *Phys. Med. Biol.*, vol. 62, no. 2, pp. 377–393, 2017, doi: 10.1088/1361-6560/aa5078.

[39]   A. F. Resch, P. D. Heyes, H. Fuchs, N. Bassler, D. Georg, and H. Palmans, "Dose-rather than fluence-averaged LET should be used as a single-parameter descriptor of proton beam quality for radiochromic film dosimetry.," *Med. Phys.*, vol. 47, no. 5, pp. 2289–2299, Jun. 2020, doi: 10.1002/mp.14097.

[40]   A. K. Jain and H. Chen, "Matching of dental X-ray images for human identification," *Pattern Recognit.*, vol. 37, no. 7, pp. 1519–1532, 2004, doi: 10.1016/j.patcog.2003.12.016.

[41]   P. Peschke, C. P. Karger, M. Scholz, J. Debus, and P. E. Huber, "Relative biological effectiveness of carbon ions for local tumor control of a radioresistant prostate carcinoma in the rat.," *Int. J. Radiat. Oncol. Biol. Phys.*, vol. 79, no. 1, pp. 239–246, Jan. 2011, doi: 10.1016/j.ijrobp.2010.07.1976.

[42]   S. Girst *et al.*, "Proton Minibeam Radiation Therapy Reduces Side Effects in an In Vivo Mouse Ear Model.," *Int. J. Radiat. Oncol. Biol. Phys.*, vol. 95, no. 1, pp. 234–241, May 2016, doi: 10.1016/j.ijrobp.2015.10.020.

[43]   E. Ford *et al.*, "An image-guided precision proton radiation platform for preclinical in vivo research.," *Phys. Med. Biol.*, vol. 62, no. 1, pp. 43–58, Jan. 2017, doi: 10.1088/1361-6560/62/1/43.

[44]   J. Daartz, M. Engelsman, H. Paganetti, and M. R. Bussière, "Field size dependence of the output factor in passively scattered proton therapy: influence of range, modulation, air gap, and machine settings.," *Med. Phys.*, vol. 36, no. 7, pp. 3205–3210, Jul. 2009, doi: 10.1118/1.3152111.

[45]   U. Titt, Y. Zheng, O. N. Vassiliev, and W. D. Newhauser, "Monte Carlo investigation

of collimator scatter of proton-therapy beams produced using the passive scattering method.," *Phys. Med. Biol.*, vol. 53, no. 2, pp. 487–504, Jan. 2008, doi: 10.1088/0031-9155/53/2/014.

[46] D. Wang, B. R. Smith, E. Gelover, R. T. Flynn, and D. E. Hyer, "A method to select aperture margin in collimated spot scanning proton therapy," *Phys. Med. Biol.*, vol. 60, no. 7, pp. N109–N119, 2015, doi: 10.1088/0031-9155/60/7/N109.

[47] A. Kacperek, "Protontherapy of eye tumours in the UK: A review of treatment at Clatterbridge," *Appl. Radiat. Isot.*, vol. 67, no. 3, pp. 378–386, 2009, doi: 10.1016/j.apradiso.2008.06.012.

[48] J. Shen *et al.*, "Impact of range shifter material on proton pencil beam spot characteristics," *Med. Phys.*, vol. 42, no. 3, pp. 1335–1340, 2015, doi: 10.1118/1.4908208.